International Journal of Solids and Structures 51 (2014) 2144–2156

Contents lists available at ScienceDirect

International Journal of Solids and Structures

journal homepage: www.elsevier.com/locate/ijsolstr

An invariant formulation for phase field models in ferroelectrics

D. Schrade [a,*], R. Müller [a], D. Gross [b], M.-A. Keip [c], H. Thai [c], J. Schröder [c]

[a] Technische Universität Kaiserslautern, Lehrstuhl für Technische Mechanik, Gottlieb-Daimler-Straße, Postfach 3049, D-67653 Kaiserslautern, Germany
[b] Technische Universität Darmstadt, FB 13, Fachgebiet Festkörpermechanik, Petersenstraße 13, D-64287 Darmstadt, Germany
[c] Universität Duisburg-Essen, Institut für Mechanik, Universitätsstraße 15, D-45141 Essen, Germany

ARTICLE INFO

Article history:
Received 23 October 2013
Received in revised form 12 February 2014
Available online 26 February 2014

Keywords:
Phase field
Ferroelectrics
Ginzburg–Landau equation
Invariant formulation

ABSTRACT

This paper introduces an electro-mechanically coupled phase field model for ferroelectric domain evolution based on an invariant formulation for transversely isotropic piezoelectric material behavior. The thermodynamic framework rests upon Gurtin's notion of a micro-force system in conjunction with an associated micro-force balance. This leads to a formulation of the second law, from which a generalized Ginzburg–Landau evolution equation is derived. The invariant formulation of the thermodynamic potential provides a consistent way to obtain the order parameter dependent elastic stiffness, piezoelectric, and dielectric tensor. The model is reduced to 2d and implemented into a finite element framework. The material constants used in the simulations are adapted to meet the thermodynamic condition of a vanishing micro-force. It is found that the thermodynamic potential taken from the literature has to be extended in order to avoid a loss of positive definiteness of the stiffness and the dielectric tensor. The small-signal response is investigated in the presence and in the absence of the additional regularizing terms in the potential. The simulations show the pathological behavior of the model in case these terms are not taken into account. The paper closes with microstructure simulations concerning a ferroelectric nanodot subjected to an electric field, a cracked single crystal, and a ferroelectric bi-crystal.

1. Introduction

Ferroelectric materials are widely used in various industrial applications, such as sensor and actuator technology, non-volatile memory devices, micro-fluidics, transducers, and many more (Scott, 2007). Their macroscopic electro-mechanical properties depend on the ferroelectric domain structure which is subject to change under externally applied loading. The evolution of the domain structure is thus a key point in understanding and engineering the macroscopic properties of ferroelectric functional devices.

Phase field modeling provides a well-established and physically sound way to simulate evolving domain structures. The models currently in use are based on a continuum thermomechanics approach which incorporates an order parameter (generally the electrical polarization) as well as its first spatial gradient. The main differences between these models lie in the choice of the order parameter, the way in which the free energy is formulated, and in the numerical solution strategy. Traditionally the order parameter is the material polarization, and the free energy function is expanded to reflect cubic symmetry conditions with respect to the primary thermodynamic variables (strain and electric displacement), see e.g. the more recent publications (Völker and Kamlah, 2012; Xu et al., 2013; Chen, 2008; Su et al., 2011; Wang and Su, 2011) and the literature review given in Schrade et al. (2013). Since in these models there is no direct coupling between the electric displacement and the mechanical strain, the piezoelectric behavior is encoded in the Landau potential which is a polynomial in the order parameter. The resulting difficulties of fitting the small-signal response to the bulk properties of the material are addressed in detail in Völker et al. (2011, 2012) Another possibility is to meet the symmetry requirements of the spontaneously polarized state and thus to include the piezoelectric coupling terms in the free energy. The Landau free energy can then be used to adjust the properties of domain walls, see Schrade et al. (2013, 2008, 2007). As for numerical solution strategies, Fourier spectral methods appear to be quite time efficient (Chen and Shen, 1998) while imposing restrictions on geometry, applicable boundary conditions, and material inhomogeneities. Another approach based on a staggered solution algorithm with explicit time integration was taken in Zhang and Bhattacharya (2005a,b). The various shortcomings of such numerical implementations can be circumvented by finite element

* Corresponding author. Tel.: +49 6312053781.
E-mail addresses: schrade@rhrk.uni-kl.de (D. Schrade), ram@rhrk.uni-kl.de (R. Müller), gross@mechanik.tu-darmstadt.de (D. Gross), marc-andre.keip@uni-due.de (M.-A. Keip), huy.thai@uni-due.de (H. Thai), j.schroeder@uni-due.de (J. Schröder).

http://dx.doi.org/10.1016/j.ijsolstr.2014.02.021
0020-7683/

implementations (however at the expense of simulation time), see e.g. Su and Landis (2007), Schrade et al. (2007) and Miehe et al. (2012).

The cited publications (Schrade et al., 2013, 2008, 2007) are however limited to an isotropic mechanical stiffness and dielectric tensor. Motivated by Keip et al. (2014), in this article we intend to overcome these shortcomings by introducing a phase field model based on an invariant formulation for transverse isotropy which is adapted to fit into the existing phase field framework. The main problem in this adaption procedure is shown to be a loss of positive definiteness of the stiffness and the dielectric tensor. This problem is solved by extending the thermodynamic potential so that the material tangent remains positive definite for arbitrary polarization states. In a second step, the small-signal model response is compared with the input parameters of the simulation model. The input parameters are then adjusted under the condition of a vanishing micro-force. Numerical examples illustrate the necessity for extending the invariant description and adjusting the input parameters.

2. Phase field model

2.1. Basic equations and thermodynamical framework

We make use of Gurtin and Fried's notion of a generalized micro-force thermodynamics (Fried and Gurtin, 1993, 1994; Gurtin, 1996) and, following (Su and Landis, 2007), apply this theory to a phase field model. Since the current thermodynamical approach is already laid out in detail in Schrade et al. (2013), we will only summarize the main aspects in this regard while trying to keep the presentation self contained.

In the presence of volume forces $\boldsymbol{f}$ and volume charges ρ the ferroelectric body $\mathcal{B}$ under consideration obeys the mechanical and electrical field equations

$$\operatorname{div}\boldsymbol{\sigma}+\boldsymbol{f}=\boldsymbol{0}, \quad \operatorname{div}\boldsymbol{D}-\rho=0, \tag{1}$$

where $\boldsymbol{\sigma}$ is the stress tensor and $\boldsymbol{D}$ is the electric displacement. The linearized strain tensor $\boldsymbol{\varepsilon}$ and the electric field $\boldsymbol{E}$ are defined by the symmetrical and the negative gradient of the displacement field $\boldsymbol{u}$ and the electric potential φ:

$$\boldsymbol{\varepsilon}=\frac{1}{2}\left(\nabla\boldsymbol{u}+(\nabla\boldsymbol{u})^{\mathrm{T}}\right), \quad \boldsymbol{E}=-\nabla\varphi. \tag{2}$$

The thermodynamic framework consists of a micro-force system involving a micro-stress tensor $\boldsymbol{\Sigma}$ and the internal and external micro-force vector $\boldsymbol{g}$ and ζ, respectively. For an arbitrary control volume $\mathcal{R}$ with boundary $\partial\mathcal{R}$ and outer unit normal $\boldsymbol{n}$ the power expenditure of each of these quantities reads

$$\int_{\partial\mathcal{R}}(\boldsymbol{\Sigma}\boldsymbol{n})\cdot\dot{\boldsymbol{P}}\,\mathrm{d}a, \quad \int_{\mathcal{R}}\boldsymbol{g}\cdot\dot{\boldsymbol{P}}\,\mathrm{d}v, \quad \int_{\mathcal{R}}\zeta\cdot\dot{\boldsymbol{P}}\,\mathrm{d}v. \tag{3}$$

The physical meaning of the order parameter $\boldsymbol{P}(\boldsymbol{x},t)$ depends on the concrete choice of the thermodynamic potential (Schrade et al., 2013). As will be shown in Section 2.2, $\boldsymbol{P}(\boldsymbol{x},t)$ here is the material polarization less its dielectric and piezoelectric parts. Changes in the order parameter reflect reorganization in the microstructure. Such reorganization is accompanied by a dissipative process and by changes in the thermodynamic potential, both of which are taken into account by the internal micro-force. Referring to Gurtin (1996), we assume the local micro-force balance

$$\operatorname{div}\boldsymbol{\Sigma}+\zeta+\boldsymbol{g}=\boldsymbol{0}. \tag{4}$$

The second law of thermodynamics balances the power expenditure of external sources with changes in the Helmholtz free energy $\Psi=\tilde{\Psi}(\boldsymbol{\varepsilon},\boldsymbol{D},\boldsymbol{P},\nabla\boldsymbol{P})$; hence we have to include $(3)_1$ and $(3)_3$ in the second law:

$$\int_{\partial\mathcal{R}}\left((\boldsymbol{\sigma}\boldsymbol{n})\cdot\dot{\boldsymbol{u}}-\varphi\frac{\mathrm{d}}{\mathrm{d}t}(\boldsymbol{D}\cdot\boldsymbol{n})+(\boldsymbol{\Sigma}\boldsymbol{n})\cdot\dot{\boldsymbol{P}}\right)\mathrm{d}a + \int_{\mathcal{R}}\left(\boldsymbol{f}\cdot\dot{\boldsymbol{u}}+\varphi\dot{\rho}+\zeta\cdot\dot{\boldsymbol{P}}\right)\mathrm{d}v-\frac{\mathrm{d}}{\mathrm{d}t}\int_{\mathcal{R}}\Psi\,\mathrm{d}v\geqslant 0. \tag{5}$$

In accordance with current ferroelectric phase field modeling, electrostatic forces (cf. McMeeking and Landis, 2005) are not taken into account so that the Cauchy stress $\boldsymbol{\sigma}$ is symmetric. After a Legendre transform of the Helmholtz free energy according to

$$H=\Psi-\boldsymbol{D}\cdot\boldsymbol{E}, \tag{6}$$

we obtain (cf. Nowacki et al., 1979) the electric enthalpy $H=\tilde{H}(\boldsymbol{\varepsilon},\boldsymbol{E},\boldsymbol{P},\nabla\boldsymbol{P})$ and write

$$\int_{\partial\mathcal{R}}\left((\boldsymbol{\sigma}\boldsymbol{n})\cdot\dot{\boldsymbol{u}}+(\boldsymbol{D}\cdot\boldsymbol{n})\dot{\varphi}+(\boldsymbol{\Sigma}\boldsymbol{n})\cdot\dot{\boldsymbol{P}}\right)\mathrm{d}a + \int_{\mathcal{R}}\left(\boldsymbol{f}\cdot\dot{\boldsymbol{u}}-\rho\dot{\varphi}+\zeta\cdot\dot{\boldsymbol{P}}\right)\mathrm{d}v-\frac{\mathrm{d}}{\mathrm{d}t}\int_{\mathcal{R}}H\,\mathrm{d}v\geqslant 0. \tag{7}$$

The internal micro-force $\boldsymbol{g}$ is omitted in the second law as it is not part of the external power supply. Combining the local form of (7) with (4), one obtains by standard arguments of rational thermomechanics

$$\boldsymbol{\sigma}=\frac{\partial H}{\partial\boldsymbol{\varepsilon}}, \quad \boldsymbol{D}=-\frac{\partial H}{\partial\boldsymbol{E}}, \quad \boldsymbol{\Sigma}=\frac{\partial H}{\partial\nabla\boldsymbol{P}}. \tag{8}$$

Insertion of these relations in the local form of the second law yields the residual dissipation inequality

$$-(\boldsymbol{g}+\boldsymbol{\eta})\cdot\dot{\boldsymbol{P}}\geqslant 0, \tag{9}$$

where

$$\boldsymbol{\eta}=\frac{\partial H}{\partial\boldsymbol{P}} \tag{10}$$

is the micro-force vector. The term in the parenthesis is identified as the dissipative micro-force

$$\boldsymbol{g}_{\mathrm{dis}}=\boldsymbol{g}+\boldsymbol{\eta}. \tag{11}$$

The residual dissipation inequality (9) is satisfied (by means of a sufficient condition) by assuming

$$\boldsymbol{g}_{\mathrm{dis}}=-\boldsymbol{\beta}\dot{\boldsymbol{P}}, \tag{12}$$

where $\boldsymbol{\beta}$ is a positive semi-definite second order inverse mobility tensor (Gurtin, 1996). The dissipation $\mathcal{D}$ which takes place due to the evolving microstructure is then given by

$$\mathcal{D}=\int_{\mathcal{B}}-\boldsymbol{g}_{\mathrm{dis}}\cdot\dot{\boldsymbol{P}}\,\mathrm{d}v=\int_{\mathcal{B}}\dot{\boldsymbol{P}}\cdot(\boldsymbol{\beta}\dot{\boldsymbol{P}})\,\mathrm{d}v\geqslant 0. \tag{13}$$

We can now see that the internal micro-force

$$\boldsymbol{g}=\boldsymbol{g}_{\mathrm{dis}}-\boldsymbol{\eta}=-\boldsymbol{\beta}\dot{\boldsymbol{P}}-\frac{\partial H}{\partial\boldsymbol{P}} \tag{14}$$

has a dissipative and a non-dissipative contribution. An evaluation of the residual dissipation inequality leads to a generalized form of the Ginzburg–Landau equation (Schrade et al., 2013):

$$\boldsymbol{\beta}\dot{\boldsymbol{P}}=\operatorname{div}\boldsymbol{\Sigma}+\zeta-\frac{\partial H}{\partial\boldsymbol{P}}. \tag{15}$$

We limit ourselves to Dirichlet and Neumann boundary conditions and neglect the vacuum polarization outside of $\mathcal{B}$:

$$\begin{aligned}&\boldsymbol{u}-\boldsymbol{u}^{*}=\boldsymbol{0} \quad \text{on } \partial\mathcal{B}_u, \boldsymbol{\sigma}\boldsymbol{n}-\boldsymbol{t}^{*}=\boldsymbol{0} \quad \text{on } \partial\mathcal{B}_\sigma,\\ &\varphi-\varphi^{*}=0 \quad \text{on } \partial\mathcal{B}_\varphi, \boldsymbol{D}\cdot\boldsymbol{n}+\rho_{\mathrm{s}}^{*}=0 \quad \text{on } \partial\mathcal{B}_D,\\ &\boldsymbol{P}-\boldsymbol{P}^{*}=\boldsymbol{0} \quad \text{on } \partial\mathcal{B}_P, \boldsymbol{\Sigma}\boldsymbol{n}-\boldsymbol{\pi}^{*}=\boldsymbol{0} \quad \text{on } \partial\mathcal{B}_\Sigma,\end{aligned} \tag{16}$$

where $\boldsymbol{t}^{*}$, ρ_{s}^{*}, and $\boldsymbol{\pi}^{*}$ are prescribed surface tractions, surface charge densities, and polarization fluxes, respectively. Initial values for the order parameter are prescribed at every material point by

$$\boldsymbol{P}(\boldsymbol{x},t)|_{t=0} = \boldsymbol{P}_0^*(\boldsymbol{x}) \quad \text{in } \mathcal{B}. \tag{17}$$

For the displacement field $\boldsymbol{u}(\boldsymbol{x},t)$ and the electric potential $\varphi(\boldsymbol{x},t)$ we prescribe the trivial initial conditions $\boldsymbol{u}(\boldsymbol{x},0)=\boldsymbol{0}$ and $\varphi(\boldsymbol{x},0)=0$.

2.2. Specification of the electric enthalpy

We use the same form of the electric enthalpy H as in our recent publication (Schrade et al., 2013) which contains a thorough discussion of the symmetry requirements regarding the Taylor expansion of the free energy/electric enthalpy. Here we consider barium titanate in the tetragonal phase and write

$$H = H^{\text{bulk}} + H^{\text{sep}} + H^{\text{grad}} \tag{18}$$

with

$$H^{\text{bulk}} = \frac{1}{2}(\boldsymbol{\varepsilon}-\boldsymbol{\varepsilon}^0)\cdot\left[\mathbb{C}(\boldsymbol{\varepsilon}-\boldsymbol{\varepsilon}^0)\right] - \left[\boldsymbol{e}(\boldsymbol{\varepsilon}-\boldsymbol{\varepsilon}^0)+\frac{1}{2}\boldsymbol{\epsilon}\boldsymbol{E}+\boldsymbol{P}\right]\cdot\boldsymbol{E}, \tag{19}$$

$$H^{\text{sep}} = \kappa_{\text{sep}}\frac{G}{\ell}\psi(\boldsymbol{P}), \tag{20}$$

$$H^{\text{grad}} = \frac{1}{2}\kappa_{\text{grad}}\frac{G\ell}{P_0^2}\|\nabla\boldsymbol{P}\|^2. \tag{21}$$

The term H^{bulk} has the form of an electric enthalpy for piezoelectric materials, except that here the material tensors $\mathbb{C},\boldsymbol{e}$, and $\boldsymbol{\epsilon}$ as well as the spontaneous eigenstrain $\boldsymbol{\varepsilon}^0$ depend on the order parameter (see the invariant formulation below). The second term H^{sep} (separation energy) is a non-convex potential which ensures that the free energy has minima at the spontaneous states. In most other phase field models for ferroelectric domain evolution this potential coincides with the Landau free energy Ψ^{Landau}. The Landau free energy typically contains all terms which only depend on $\boldsymbol{P}$ and not on any other primary thermodynamic variable such as $\boldsymbol{D}$ or $\boldsymbol{\varepsilon}$. Since in (19) the elastic stiffness and the spontaneous strain both depend on $\boldsymbol{P}$ (see below), the separation potential H^{sep} and the Landau free energy do not coincide but are related through

$$\Psi^{\text{Landau}} = H^{\text{sep}} + \frac{1}{2}\boldsymbol{\varepsilon}^0\cdot(\mathbb{C}\boldsymbol{\varepsilon}^0). \tag{22}$$

The local characteristics of H^{sep} are encoded in the normalized non-convex function ψ (see below). Finally the term H^{grad} is the order parameter gradient energy.

In (20) and (21) the regularization parameter ℓ is the 180° domain wall width and G is the specific domain wall energy originating from H^{sep} and H^{grad}; κ_{sep} and κ_{grad} are dimensionless calibration constants which ensure that G and ℓ can be interpreted in this way not just qualitatively but also quantitatively, see Schrade et al. (2013) for a detailed justification. The constant P_0 is the spontaneous polarization of the unloaded crystal. Due to (8) the constitutive equations take the form

$$\boldsymbol{\sigma} = \mathbb{C}(\boldsymbol{\varepsilon}-\boldsymbol{\varepsilon}^0) - \boldsymbol{e}^{\mathrm{T}}\boldsymbol{E}, \tag{23}$$

$$\boldsymbol{D} = \boldsymbol{e}(\boldsymbol{\varepsilon}-\boldsymbol{\varepsilon}^0) + \boldsymbol{\epsilon}\boldsymbol{E} + \boldsymbol{P}, \tag{24}$$

$$\boldsymbol{\Sigma} = \kappa_{\text{grad}}\frac{G\ell}{P_0^2}\nabla\boldsymbol{P}, \tag{25}$$

and the evolution Eq. (15) now reads

$$\boldsymbol{\beta}\dot{\boldsymbol{P}} = \kappa_{\text{grad}}\frac{G\ell}{P_0^2}\Delta\boldsymbol{P} - \kappa_{\text{sep}}\frac{G}{\ell}\frac{\partial\psi}{\partial\boldsymbol{P}} - \frac{\partial H^{\text{bulk}}}{\partial\boldsymbol{P}} + \boldsymbol{\zeta}, \tag{26}$$

where Δ denotes the Laplace operator. Note that with (6) the corresponding Helmholtz free energy reads

$$\begin{aligned}\tilde{\Psi}(\boldsymbol{\varepsilon},\boldsymbol{D},\boldsymbol{P},\nabla\boldsymbol{P}) = {}& \frac{1}{2}\left[\boldsymbol{\epsilon}^{-1}(\boldsymbol{D}-\boldsymbol{e}(\boldsymbol{\varepsilon}-\boldsymbol{\varepsilon}^0)-\boldsymbol{P})\right]\\ & \cdot(\boldsymbol{D}-\boldsymbol{e}(\boldsymbol{\varepsilon}-\boldsymbol{\varepsilon}^0)-\boldsymbol{P}) + \frac{1}{2}(\boldsymbol{\varepsilon}-\boldsymbol{\varepsilon}^0)\\ & \cdot\left[\mathbb{C}(\boldsymbol{\varepsilon}-\boldsymbol{\varepsilon}^0)\right] + \kappa_{\text{sep}}\frac{G}{\ell}\psi(\boldsymbol{P}) + \frac{1}{2}\kappa_{\text{grad}}\\ & \times\frac{G\ell}{P_0^2}\|\nabla\boldsymbol{P}\|^2.\end{aligned} \tag{27}$$

We already mentioned that the physical interpretation of the order parameter $\boldsymbol{P}(\boldsymbol{x},t)$ depends on the specific choice of the thermodynamic potential. In view of the resulting material Eq. (24), the order parameter here is the material polarization less the piezoelectric and dielectric contributions. In most other phase field models for ferroelectrics there is no direct coupling between the mechanical strain and the electric field in the electric enthalpy, and the dielectric tensor $\boldsymbol{\epsilon}$ is taken as the vacuum permittivity. Consequently in these models the order parameter is the total material polarization.

As pointed out above, in our recent publications we only considered an isotropic elastic stiffness and dielectric tensor. Motivated by Schröder and Gross (2004) and Keip et al. (2014) we elaborate the mechanical stiffness $\mathbb{C}(\boldsymbol{P})$, the dielectric tensor $\boldsymbol{\epsilon}(\boldsymbol{P})$, and the piezoelectric constants $\boldsymbol{e}(\boldsymbol{P})$ by means of an invariant formulation for transversely isotropic material behavior. In the linear theory of piezoelectricity presented in Schröder and Gross (2004) the preferred direction $\boldsymbol{p}$ is determined by a given crystallographic axis, which is used to construct the structural tensor and the invariant basis. Generally, on the microscopic level the local anisotropy depends on the symmetry and the orientation of the crystal lattice. In this paper we use the order parameter to define the preferred direction $\boldsymbol{p}$ which is then used to construct an invariant basis for transverse isotropy. The use of $\boldsymbol{P}/|\boldsymbol{P}|$ for $\boldsymbol{p}$ is not feasible in the phase field approach since the order parameter is allowed to become zero, as for example in the case of a 180° domain wall. Instead we define the preferred direction $\boldsymbol{p}$ and the structural tensor $\mathbf{m}$ by

$$\boldsymbol{p} = \frac{\boldsymbol{P}}{P_0}, \quad \mathbf{m} = \boldsymbol{p}\otimes\boldsymbol{p}, \tag{28}$$

which is well defined for arbitrary values of $\boldsymbol{P}$. Note that this definition of the preferred direction in terms of the order parameter is only applicable for ferroelectric crystals in which the polar axes coincide with the crystallographic axes, e.g. tetragonal $BaTiO_3$. For other crystals which do not satisfy this requirement one would have to find some other way to connect the crystallographic axes to the order parameter or employ an altogether different approach.

As we will see below, this choice of the preferred direction implies that the material tensors $\mathbb{C},\boldsymbol{e}$, and $\boldsymbol{\epsilon}$ change as the order parameter evolves in time (e.g. due to external loading). This point is addressed in Section 3.2, where the small-signal response of the model is calibrated for a vanishing micro-force vector so that the changes in these material constants are effectively taken into account. Moreover, the use of $\boldsymbol{P}/|\boldsymbol{P}|$ as the preferred direction causes severe numerical problems when $|\boldsymbol{P}|/P_0 \ll 1$ (cf. Section 3.5). Then the time step required to achieve convergence has to be reduced by about eight orders of magnitude which is tantamount to halting the simulation altogether. Having defined a preferred direction, we can represent the bulk enthalpy (19) as

$$\begin{aligned}H^{\text{bulk}} = {}& \frac{1}{2}\lambda I_1^2 + \mu I_2 + (\omega^{n_1}\alpha_1 + \omega^{n_6}\alpha_6)I_5 + (\omega^{n_2}\alpha_2 + \omega^{n_4}\alpha_4)I_4^2\\ & + (\omega^{n_3}\alpha_3 + \omega^{n_5}\alpha_5)I_1I_4 + \omega\beta_1I_1J_2 + \beta_2I_4J_2 + \omega\beta_3K_1\\ & + (\gamma_1+\omega\gamma_3)J_1 + \gamma_2J_2^2 + \gamma' J_2\end{aligned} \tag{29}$$

with $\omega := \operatorname{tr}\mathbf{m} = |\boldsymbol{p}|^2$, $n_i \in \mathbb{N}_0$, and the invariants

$$I_1 = \mathrm{tr}(\boldsymbol{\varepsilon} - \boldsymbol{\varepsilon}^0), \quad I_2 = \mathrm{tr}[(\boldsymbol{\varepsilon} - \boldsymbol{\varepsilon}^0)^2],$$
$$I_3 = \mathrm{tr}[(\boldsymbol{\varepsilon} - \boldsymbol{\varepsilon}^0)^3], \quad I_4 = \mathrm{tr}[(\boldsymbol{\varepsilon} - \boldsymbol{\varepsilon}^0)\mathbf{m}],$$
$$I_5 = \mathrm{tr}[(\boldsymbol{\varepsilon} - \boldsymbol{\varepsilon}^0)^2\mathbf{m}], \quad J_1 = \mathrm{tr}(\boldsymbol{E} \otimes \boldsymbol{E}),$$
$$J_2 = \mathrm{tr}(\boldsymbol{E} \otimes \boldsymbol{p}), \quad K_1 = \mathrm{tr}[(\boldsymbol{\varepsilon} - \boldsymbol{\varepsilon}^0)(\boldsymbol{E} \otimes \boldsymbol{p})], \tag{30}$$

where $\mathrm{tr}(\cdot)$ is the trace operator. Note that the invariant I_3 is not used in the linear theory of piezoelectricity. The spontaneous strain $\boldsymbol{\varepsilon}^0(\boldsymbol{P})$ reflects the tetragonal symmetry of the poled material and is given by

$$\boldsymbol{\varepsilon}^0(\boldsymbol{P}) = \varepsilon_a \mathbf{1}\omega + (\varepsilon_c - \varepsilon_a)\mathbf{m} \tag{31}$$

with

$$\varepsilon_a = (a_{tet} - a_{cub})/a_{cub}, \quad \varepsilon_c = (c_{tet} - a_{tet})/a_{cub}. \tag{32}$$

The parameters a_{cub}, a_{tet} and c_{tet} are the lattice constants of the cubic and the tetragonal phase. This formulation differs from the invariant formulation for piezoelectric materials given in Schröder and Gross (2004) in several ways. Here the invariant basis (30) contains the spontaneous strain $\boldsymbol{\varepsilon}^0$, and the bulk enthalpy (29) is extended by the terms with $\alpha_4, \alpha_5, \alpha_6$, and γ_3 which are needed to regularize the stiffness and the dielectric tensor (see below). Further, the term $\gamma' J_2$ represents the term $-\boldsymbol{P} \cdot \boldsymbol{E}$ in (19).

The material constants in (29) are expressed in terms of the "classic" constants by

$$\lambda = c_{12}, \quad \mu = \frac{1}{2}(c_{11} - c_{12}),$$
$$\alpha_1 = \begin{cases} 2c_{44} + c_{12} - c_{11} & \text{if } 2c_{44} + c_{12} - c_{11} > 0 \\ -c_{11} & \text{if } 2c_{44} + c_{12} - c_{11} < 0 \end{cases},$$
$$\alpha_6 = \begin{cases} 0 & \text{if } 2c_{44} + c_{12} - c_{11} > 0 \\ 2c_{44} + c_{12} & \text{if } 2c_{44} + c_{12} - c_{11} < 0 \end{cases},$$
$$\alpha_2 = \begin{cases} \frac{1}{2}(c_{11} + c_{33}) - 2c_{44} - c_{13} & \text{if } \frac{1}{2}(c_{11} + c_{33}) - 2c_{44} - c_{13} > 0 \\ \frac{1}{2}c_{11} - 2c_{44} - c_{13} & \text{if } \frac{1}{2}(c_{11} + c_{33}) - 2c_{44} - c_{13} < 0 \end{cases},$$
$$\alpha_4 = \begin{cases} 0 & \text{if } \frac{1}{2}(c_{11} + c_{33}) - 2c_{44} - c_{13} > 0 \\ \frac{1}{2}c_{33} & \text{if } \frac{1}{2}(c_{11} + c_{33}) - 2c_{44} - c_{13} < 0 \end{cases},$$
$$\alpha_3 = \begin{cases} c_{13} - c_{12} & \text{if } c_{13} > c_{12} \\ -c_{12} & \text{if } c_{13} < c_{12} \end{cases},$$
$$\alpha_5 = \begin{cases} 0 & \text{if } c_{13} > c_{12} \\ c_{13} & \text{if } c_{13} < c_{12} \end{cases},$$
$$\gamma_1 = \begin{cases} -\frac{1}{2}\bar{\epsilon}_{11} & \text{if } \bar{\epsilon}_{11} < \bar{\epsilon}_{33} \\ -\frac{1}{2}\bar{\epsilon}_{33} & \text{if } \bar{\epsilon}_{11} > \bar{\epsilon}_{33} \end{cases},$$
$$\gamma_3 = \begin{cases} 0 & \text{if } \bar{\epsilon}_{11} < \bar{\epsilon}_{33} \\ \frac{1}{2}(\bar{\epsilon}_{33} - \bar{\epsilon}_{11}) & \text{if } \bar{\epsilon}_{11} > \bar{\epsilon}_{33} \end{cases},$$
$$\gamma_2 = \frac{1}{2}(\bar{\epsilon}_{11} - \bar{\epsilon}_{33}), \quad \gamma' = P_0,$$
$$\beta_1 = -\bar{e}_{31}, \quad \beta_2 = -\bar{e}_{33} + 2\bar{e}_{15} + \bar{e}_{31}, \quad \beta_3 = -2\bar{e}_{15}, \tag{33}$$

where the overbar is used to distinguish between the values of material constants and the respective components of $\boldsymbol{\epsilon}$ and $\boldsymbol{e}$. Inserting (29) in (8) we obtain the constitutive equations in the form

$$\begin{aligned}\boldsymbol{\sigma} &= \frac{\partial H^{bulk}}{\partial \boldsymbol{\varepsilon}} = \sum_{k=1/3}^{5} \frac{\partial H^{bulk}}{\partial I_k}\frac{\partial I_k}{\partial \boldsymbol{\varepsilon}} + \frac{\partial H^{bulk}}{\partial K_1}\frac{\partial K_1}{\partial \boldsymbol{\varepsilon}} \\ &= \lambda I_1 \frac{\partial I_1}{\partial \boldsymbol{\varepsilon}} + \mu \frac{\partial I_2}{\partial \boldsymbol{\varepsilon}} + (\omega^{n_1}\alpha_1 + \omega^{n_6}\alpha_6)\frac{\partial I_5}{\partial \boldsymbol{\varepsilon}} + 2I_4\frac{\partial I_4}{\partial \boldsymbol{\varepsilon}} \\ &\quad \times (\omega^{n_2}\alpha_2 + \omega^{n_4}\alpha_4) + (\omega^{n_3}\alpha_3 + \omega^{n_5}\alpha_5)\left(I_4\frac{\partial I_1}{\partial \boldsymbol{\varepsilon}} + I_1\frac{\partial I_4}{\partial \boldsymbol{\varepsilon}}\right) \\ &\quad + \omega\beta_1 J_2\frac{\partial I_1}{\partial \boldsymbol{\varepsilon}} + \beta_2 J_2\frac{\partial I_4}{\partial \boldsymbol{\varepsilon}} + \omega\beta_3\frac{\partial K_1}{\partial \boldsymbol{\varepsilon}}\end{aligned} \tag{34}$$

and

$$\begin{aligned}\boldsymbol{D} &= -\frac{\partial H^{bulk}}{\partial \boldsymbol{E}} = \sum_{k=1}^{2} -\frac{\partial H^{bulk}}{\partial J_k}\frac{\partial J_k}{\partial \boldsymbol{E}} - \frac{\partial H^{bulk}}{\partial K_1}\frac{\partial K_1}{\partial \boldsymbol{E}} \\ &= -(\gamma_1 + \omega\gamma_3)\frac{\partial J_1}{\partial \boldsymbol{E}} - 2\gamma_2 J_2\frac{\partial J_2}{\partial \boldsymbol{E}} - \gamma'\frac{\partial J_2}{\partial \boldsymbol{E}} - \omega\beta_1 I_1\frac{\partial J_2}{\partial \boldsymbol{E}} - \beta_2 I_4 \\ &\quad \times \frac{\partial J_2}{\partial \boldsymbol{E}} - \omega\beta_3\frac{\partial K_1}{\partial \boldsymbol{E}}.\end{aligned} \tag{35}$$

The elastic, piezoelectric, and dielectric moduli are then given by

$$\begin{aligned}\mathbb{C}(\boldsymbol{P}) &= \frac{\partial \boldsymbol{\sigma}}{\partial \boldsymbol{\varepsilon}} = \frac{\partial}{\partial \boldsymbol{\varepsilon}}\sum_{i=1/3}^{5}\frac{\partial H^{bulk}}{\partial I_i}\frac{\partial I_i}{\partial \boldsymbol{\varepsilon}} = \lambda \mathbf{1} \otimes \mathbf{1} + 2\mu\mathbb{1} \\ &\quad + (\omega^{n_1}\alpha_1 + \omega^{n_6}\alpha_6)\Xi + 2(\omega^{n_2}\alpha_2 + \omega^{n_4}\alpha_4)\mathbf{m} \otimes \mathbf{m} \\ &\quad + (\omega^{n_3}\alpha_3 + \omega^{n_5}\alpha_5)(\mathbf{1} \otimes \mathbf{m} + \mathbf{m} \otimes \mathbf{1}),\end{aligned} \tag{36}$$

$$\begin{aligned}\boldsymbol{e}(\boldsymbol{P}) &= \frac{\partial \boldsymbol{D}}{\partial \boldsymbol{\varepsilon}} = \frac{\partial}{\partial \boldsymbol{\varepsilon}}\left(-\frac{\partial H^{bulk}}{\partial J_2}\frac{\partial J_2}{\partial \boldsymbol{E}} - \frac{\partial H^{bulk}}{\partial K_1}\frac{\partial K_1}{\partial \boldsymbol{E}}\right) \\ &= -\omega\beta_1 \boldsymbol{p} \otimes \mathbf{1} - \beta_2 \boldsymbol{p} \otimes \mathbf{m} - \omega\beta_3 \hat{\boldsymbol{e}},\end{aligned} \tag{37}$$

$$\boldsymbol{\epsilon}(\boldsymbol{P}) = \frac{\partial \boldsymbol{D}}{\partial \boldsymbol{E}} = -\frac{\partial}{\partial \boldsymbol{E}}\sum_{i=1}^{2}\frac{\partial H^{bulk}}{\partial J_i}\frac{\partial J_i}{\partial \boldsymbol{E}} = -2(\gamma_1 + \omega\gamma_3)\mathbf{1} - 2\gamma_2\mathbf{m}, \tag{38}$$

where $\mathbb{1}_{ijkl} = \frac{1}{2}(\delta_{ik}\delta_{jl} + \delta_{il}\delta_{jk})$ and $\Xi_{ijkl} = p_i\delta_{jk}p_l + p_k\delta_{il}p_j$ and $\hat{e}_{kij} = \frac{1}{2}(\delta_{ik}p_j + \delta_{jk}p_i)$. The material tensors $\mathbb{C}, \boldsymbol{e}$, and $\boldsymbol{\epsilon}$ are nonlinear polynomials in the normalized order parameter $\boldsymbol{p} = \boldsymbol{P}/P_0$. For the dielectric tensor $\boldsymbol{\epsilon}$ a polynomial of degree 2 (with a constant and quadratic term) suffices since there are only two independent permittivities. The electric enthalpy yields a dielectric tensor $\boldsymbol{\epsilon}(\boldsymbol{P})$ which stays positive definite for arbitrary values for $\boldsymbol{P}$, see Section 3.3 for details. The situation is more complicated for the piezoelectric tensor $\boldsymbol{e}(\boldsymbol{P})$ and the mechanical stiffness $\mathbb{C}(\boldsymbol{P})$. For $\boldsymbol{e}$ we have the three material parameters $\beta_1, \beta_2, \beta_3$ and a polynomial of third degree which has no constant and no quadratic term due to the factor $\omega = |\boldsymbol{p}|^2$ in the β_1- and β_3-term. If the factor ω in front of one of these terms was omitted, then there would be a linear term in the polynomial. Here we chose to include the two factors ω so that $\partial_{\boldsymbol{p}}\boldsymbol{e}(\boldsymbol{p}) = \boldsymbol{0}$ at $\boldsymbol{p} = \boldsymbol{0}$. Otherwise there may be local extrema in the component e_{333}, depending on the values of the material parameters β_1 and β_3.

For the mechanical stiffness $\mathbb{C}$ we have a polynomial of at least forth degree. If the polarization direction is assumed to be the x_1-axis, i.e. if $p_2 = p_3 = 0$ and hence $\omega = p_1^2$, then one obtains according to (36)

$$\begin{aligned}\mathbb{C}_{1111} &= \lambda + 2\mu + 2(\omega^{n_1}\alpha_1 + \omega^{n_6}\alpha_6)p_1^2 + 2(\omega^{n_2}\alpha_2 \\ &\quad + \omega^{n_4}\alpha_4)p_1^4 + 2(\omega^{n_3}\alpha_3 + \omega^{n_5}\alpha_5)p_1^2,\end{aligned} \tag{39}$$

$$\mathbb{C}_{1133} = \lambda + 2(\omega^{n_3}\alpha_3 + \omega^{n_5}\alpha_5)p_1^2, \tag{40}$$

$$\tilde{\mathbb{C}}_{1313} = \frac{1}{2}(\mathbb{C}_{1313} + \mathbb{C}_{1331}) = \mu + \frac{1}{2}(\omega^{n_1}\alpha_1 + \omega^{n_6}\alpha_6)p_1^2, \tag{41}$$

$$\mathbb{C}_{3333} = c_{11}, \quad \mathbb{C}_{2233} = c_{12}, \quad \tilde{\mathbb{C}}_{2323} = \frac{1}{2}(\mathbb{C}_{2323} + \mathbb{C}_{2332}) = \mu. \tag{42}$$

The additional terms with α_5 and α_6 are necessary if $c_{13} - c_{12} < 0$ and $2c_{44} + c_{12} - c_{11} < 0$, respectively, since in this case the coefficient of the term of the highest order would have a negative sign so that the stiffnesses would become zero at some point with $|\boldsymbol{p}| > 1$. With $n_6 > n_1$ and $n_5 > n_2$ and the definitions in (33) the coefficient of the highest-order terms in (40) and (41) are guaranteed to be positive. The additional term with α_4 becomes necessary if the coefficient of the highest-order term in (39) is negative. This can be the case if $\frac{1}{2}(c_{11} + c_{33}) - 2c_{44} - c_{13} < 0$. The addition of the α_4-term then ensures that the coefficient of the highest-order polynomial is positive as long as $n_4 > n_2$. Once

the necessity for the α_4, α_5, and α_6-terms is assessed, the exponents n_i are used to adjust the locations of the minima of the stiffness components which are a polynomial of degree 4 or higher.

Fig. 1 shows the stiffness components $\mathbb{C}_{1111}$, $\mathbb{C}_{1133}$, and $\tilde{\mathbb{C}}_{1313}$ for $BaTiO_3$, PZT and PTO. The material parameters for $BaTiO_3$ are given in (51), (52) and Table 2 ("adjusted values"); the values for PZT and PTO (see Table 1) are given in Völker et al. (2012), p. 5, and originate from first-principles DFT simulations cited therein. The graphs for $BaTiO_3$ in Fig. 1(a) and (b) are obtained with $n_1 = 1,\ n_2 = 0,\ n_3 = 0,\ n_4 = 1,$ and $\alpha_5 = \alpha_6 = 0$. This gives the stiffness tensor

$$\mathbb{C}(\boldsymbol{P}) = \lambda \mathbf{1}\otimes\mathbf{1} + 2\mu\mathbb{1} + \omega\alpha_1\Xi + 2(\alpha_2+\omega\alpha_4)\mathbf{m}\otimes\mathbf{m} + \alpha_3(\mathbf{1}\otimes\mathbf{m}+\mathbf{m}\otimes\mathbf{1}). \tag{43}$$

Note that according to the definition of the parameters α_i in (33) there should be a term with α_5 for the adjusted $BaTiO_3$ parameters for which $c_{13} < c_{12}$. However, since the difference of the these two values is relatively small, we may keep the same electric enthalpy and hence the same stiff tensor for both sets of $BaTiO_3$ material parameters and accept that $\mathbb{C}_{1133}$ vanishes at some point far away from $p_1 = \pm 1$. This is not problematic since $|\boldsymbol{p}|$ can well be expected to stay within the given plotting interval. Note that if desired, one could include the α_5-term and obtain a positive $\mathbb{C}_{1133}$ for all p_1. The graphs in Fig. 1(c) and (d) were obtained by using for PZT: $n_1 = 3,\ n_2 = 2,\ n_3 = 1,\ n_4 = 3$ and $n_6 = 4$ ($\alpha_5 = 0$ so that n_5 does not occur in the potential); for PTO $n_1 = 5,\ n_2 = 0,\ n_3 = 2,\ n_4 = 1,\ n_5 = 3$, and $n_6 = 6$ was used. Due to the inclusion of the α_4-, α_5-, and α_6-terms the stiffness tensors can be regularized; without these terms some components of $\mathbb{C}$ would become close to zero within the plotting interval so that positive definiteness would not be given.

To summarize this elaboration: The additional terms with α_4, α_5, and α_6 are used to regularize the stiffness tensor. The need of any of these three terms is determined by the definition of the material parameters in (33). The shape of the curves shown in Fig. 1 can be adjusted with the free exponents n_i so that the minima of the graphs are close to the spontaneous states at $p_1 = \pm 1$. This has been done here exemplarily for $BaTiO_3$, PZT and PTO material data; it can be expected that the adaption process can also be undertaken for other ferroelectric materials with tetragonal symmetry.

Table 1
Elastic constants for PZT and PTO in 10^{10} N/m^2 according to Völker et al. (2012).

	c_{11}	c_{33}	c_{12}	c_{13}	c_{44}
PZT	32.7	17.8	11.4	11.9	7.3
PTO	28.5	9.1	11.9	8.8	6.5

Table 2
The adjusted material parameter values yield numerical tangent moduli which match the original input values.

	Input values	Response	Adjusted values	Response	Units
c_{11}	22.2	21.6	23.05	22.2	
c_{33}	15.1	14.6	15.75	15.1	
c_{12}	10.8	–	10.8	–	10^{10} N/m^2
c_{13}	11.1	11.6	10.4	11.1	
c_{44}	6.1	4.03	12.67	6.10	
$\bar{e}_{31}$	−0.7	−2.14	+1.327	−0.700	
$\bar{e}_{33}$	6.7	7.93	4.96	6.70	C/m^2
$\bar{e}_{15}$	34.2	27.0	57	34.2	
$\bar{\epsilon}_{11}$	19.5	22.0	11.6	19.5	
$\bar{\epsilon}_{33}$	0.496	0.832	0.209	0.496	10^{-9} C/(Vm)

The 3d version of the dimensionless non-convex potential $\psi(\boldsymbol{P})$ in (20) is assumed to take the form

$$\psi(\boldsymbol{P}) = \psi_0 + \frac{\psi_1}{P_0^2}\left(P_1^2+P_2^2+P_3^2\right) + \frac{\psi_2}{P_0^4}\left(P_1^4+P_2^4+P_3^4\right) + \frac{\psi_3}{P_0^4}\left(P_1^2P_2^2+P_1^2P_3^2+P_2^2P_3^2\right) + \frac{\psi_4}{P_0^6}\left(P_1^6+P_2^6+P_3^6\right). \tag{44}$$

Note that the two representations of the bulk enthalpy (19) and (29) are equivalent. The advantage of the former lies in its clarity as it formally reflects classic piezoelectric theory, while the latter provides a consistent way to implement the desired transversely isotropic symmetry conditions in the theoretical model.

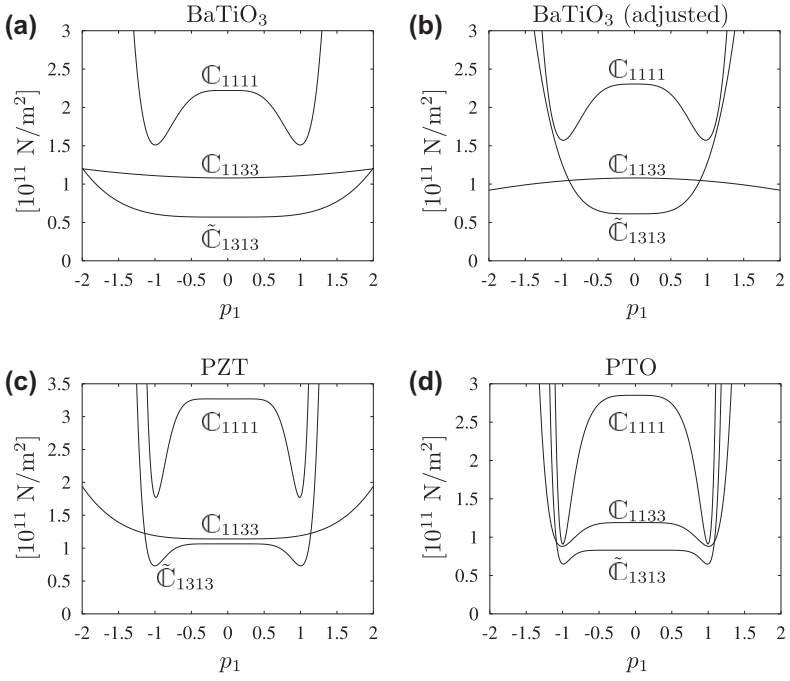

Fig. 1. Plots of the three order parameter dependent stiffness components along $\boldsymbol{p} = [p_1, 0, 0]^T$.

The five coefficients ψ_j are determined by postulating

$$\psi(0,0,0)=1,\quad \psi(P_0,0,0)=0,\quad \frac{\partial\psi(P_0,0,0)}{\partial P_1}=0,\quad \psi(\xi P_0,\xi P_0,0)=\psi_{90},\quad \frac{\partial\psi(\xi P_0,\xi P_0,0)}{\partial P_1}=0, \tag{45}$$

which introduces the relative energy barrier for 90° switching ψ_{90} as well as its location ξ in the energy landscape ψ. These equations yield a linear system of equations, the solution of which is

$$\psi_1=-\frac{1-\psi_{90}-2\xi^6}{\xi^2(1-\xi^4)},\quad \psi_2=-\frac{-2(1-\psi_{90})+3\xi^2+\xi^6}{\xi^2(1-\xi^4)},$$
$$\psi_3=\frac{-2\xi^6+6\xi^4-3\xi^2+3\xi^2\psi_{90}+1-\psi_{90}}{\xi^4(1+\xi^2)},\quad \psi_4=\frac{2\xi^2+\psi_{90}-1}{\xi^2(1-\xi^4)}. \tag{46}$$

Since we intend ψ to have minima only at the spontaneous states, we must observe the restrictions $\psi_1<0\leqslant\psi_4$ which implies

$$\sqrt{\frac{1-\psi_{90}}{2}}\leqslant\xi<\sqrt[6]{\frac{1-\psi_{90}}{2}}\quad\text{with}\quad 0<\psi_{90}<1. \tag{47}$$

The calibration constants κ_{sep} and κ_{grad} are given by

$$\kappa_{\text{sep}}^{-1}=\frac{1}{2}\kappa_{\text{grad}}^{-1}=\int_{-1}^{1}\sqrt{\psi_0+\psi_1 q^2+\psi_2 q^4+\psi_4 q^6}\,\mathrm{d}q. \tag{48}$$

A detailed account of the construction of ψ and the determination of κ_{sep} and κ_{grad} can be found in Schrade et al. (2013).

3. 2d numerical simulations

We reduce the presented model to 2d with respect to the x_2-direction. The reduction procedure is described at length in Schrade et al. (2013), so without further discussion we set

$$E_2:=0,\quad P_2:=0,\quad \varepsilon_{22}:=\varepsilon_{22}^0=\varepsilon_{\text{a}},\quad \varepsilon_{12}=\varepsilon_{21}=\varepsilon_{23}=\varepsilon_{32}:=0. \tag{49}$$

This results in the non-vanishing stress

$$\sigma_{22}=c_{12}(\varepsilon_{11}-\varepsilon_{11}^0)+c_{13}(\varepsilon_{33}-\varepsilon_{33}^0). \tag{50}$$

As a consequence of the reduction, the components $\sigma_{ij}, D_i, \varepsilon_{ij}, \varepsilon_{ij}^0$, and Σ_{ij} vanish if $i=2$ or $j=2$ (except for σ_{22}).

The 2d model with the PDEs in (1) and the Ginzburg–Landau Eq. (26), which are supplemented by (2), (19), (23), (24), (36), (37), and the boundary and initial conditions (16) and (17), are numerically solved using a 2d implementation in the finite element code FEAP (Taylor et al., 2013). Within an isoparametric concept, 4-noded plane elements with bilinear ansatz functions are used to discretize the body $\mathcal{B}$ as well as the nodal variables $\boldsymbol{u}, \varphi$, and the order parameter $\boldsymbol{P}$. Time discretization is implemented by means of the first order implicit Euler method, and the occurring element integrals are approximated by using 4-point Gauss integration. A detailed description of the numerical implementation can be found in D. Schrade et al. (2011).

3.1. Material parameters

The single crystal $BaTiO_3$ bulk material constants are taken from Zgonik et al. (1994); the spontaneous polarization and the lattice constants are given in Xu (1991) and Jona and Shirane (1993). In short we have

$$c_{11}=22.2\cdot10^{10}\,\text{Nm}^{-2},\quad c_{33}=15.1\cdot10^{10}\,\text{Nm}^{-2},\quad c_{12}=10.8\cdot10^{10}\,\text{Nm}^{-2}, \tag{51}$$

$$c_{13}=11.1\cdot10^{10}\,\text{Nm}^{-2},\quad c_{44}=6.1\cdot10^{10}\,\text{Nm}^{-2}, \tag{52}$$

$$\bar{e}_{31}=-0.7\,\text{Cm}^{-2},\quad \bar{e}_{33}=6.7\,\text{Cm}^{-2},\quad \bar{e}_{15}=34.2\,\text{Cm}^{-2}, \tag{53}$$

$$\bar{\epsilon}_{11}=19.5\cdot10^{-9}\,(\text{Vm})^{-1},\quad \bar{\epsilon}_{33}=0.496\cdot10^{-9}\,(\text{Vm})^{-1}, \tag{54}$$

$$a_{\text{cub}}=4.01\,\text{Å},\quad a_{\text{tet}}=3.992\,\text{Å},\quad c_{\text{tet}}=4.032\,\text{Å}, \tag{55}$$

$$P_0=0.26\,\text{Cm}^{-2}. \tag{56}$$

The lattice parameters have been evaluated at room temperature. Since there is no stable cubic phase at that temperature the value for a_{cub} was taken at the tetragonal-cubic transition point. Note that one might assume an extrapolated value for the cubic lattice parameter at room temperature. Referring to Jona and Shirane (1993) this would give $a_{\text{cub}}=4.005$ Å and would lead to differences in spontaneous strain of $\Delta\varepsilon_{\text{a}}=-0.124\%$ and $\Delta\varepsilon_{\text{c}}=-0.125\%$. These differences have an influence on the domain wall energy contribution from H^{bulk}. For the microstructure evolution presented in Section 3.5 the results are quite similar, see the discussion in that section. Here we use the values given in (55). The specific 180° domain wall energy in $BaTiO_3$ was calculated in Padilla et al. (1996) by *ab initio* simulations. The values provided therein range from 4 mJ/m^2 to 17 mJ/m^2, depending on what is to be understood as "domain wall energy" in the context of first principles calculations. The width of a 180° interface is commonly estimated to be a few unit cells (Merz, 1954; Stemmer et al., 1995; Foeth et al., 1999). Here we use

$$G=12\,\text{mJ/m}^2\quad\text{and}\quad \ell=1.5\,\text{nm}. \tag{57}$$

The inverse mobility $\boldsymbol{\beta}^{-1}$ is assumed to be isotropic, and its value is taken to be

$$\beta^{-1}=\frac{2P_0}{\ell}\beta_0^{-1}=\frac{26}{75}\frac{\text{kA}}{\text{Vm}}\quad\text{with}\quad \beta_0^{-1}=10^{-6}\frac{\text{m}^2}{\text{Vs}}. \tag{58}$$

This parameter has the function of an internal time scale. As is shown in Schrade et al. (2013), it is connected with the speed of the 180° interface at constant electric loading. The chosen value leads to an interface velocity of 1 m/s for an electric field of 10^6 V/m applied parallel to the interface. The constants ψ_i in (44) are determined by the choice $\psi_{90}=0.7$ and $\xi=0.5$ in (46). Thus we have

$$\psi_0=1,\quad \psi_1=-\frac{86}{75},\quad \psi_2=-\frac{53}{75},\quad \psi_3=\frac{134}{25},\quad \psi_4=\frac{64}{75}. \tag{59}$$

From these values the calibration constants κ_{sep} and κ_{grad} are calculated according to (48) which gives

$$\kappa_{\text{sep}}\approx0.695134,\quad \kappa_{\text{grad}}\approx0.347567. \tag{60}$$

3.2. Small-signal response

Before the presented model can be used for microstructural simulations, we ought to raise the following two questions. Firstly, how does the evolving order parameter under small-signal mechanical and electric loading affect the model response, and, secondly, how can we guarantee that the dielectric and the mechanical stiffness tensors are positive definite for arbitrary values of the order parameter? The first question is addressed in this subsection; the second is investigated in Section 3.3.

The material tangent in the small-signal range around the spontaneously polarized state can be determined form the bulk enthalpy function (19). Starting with the homogeneously polarized state $\boldsymbol{P}=[0,0,P_0]^{\text{T}}$, we perform a numerical variation procedure with respect to the components of $\boldsymbol{\varepsilon}$ and $\boldsymbol{E}$. Due to homogeneous conditions the gradient of $\boldsymbol{P}$ and hence the micro-stress tensor vanish identically. By assumption there shall be no external micro-forces $\boldsymbol{\zeta}$ so that the micro-force balance (4) trivially yields $\boldsymbol{g}\equiv\boldsymbol{0}$. The residual dissipation inequality (9) then reduces to $-\boldsymbol{\eta}\cdot\boldsymbol{P}\geqslant0$,

and the question is whether the material tangent should be computed for $\mathrm{d}\boldsymbol{P}=\boldsymbol{0}$ or $\mathrm{d}\boldsymbol{\eta}=\boldsymbol{0}$. The first of these options yields the tangent moduli

$$\mathbb{C}^{E,P}=\left.\frac{\partial^2 H^{\text{bulk}}}{\partial\boldsymbol{\varepsilon}^2}\right|_{\mathrm{d}E_i=\mathrm{d}P_i=0},\quad \boldsymbol{\epsilon}^{\varepsilon,P}=-\left.\frac{\partial^2 H^{\text{bulk}}}{\partial\boldsymbol{E}^2}\right|_{\mathrm{d}\varepsilon_{ij}=\mathrm{d}P_i=0},$$
$$\boldsymbol{e}^{P}=-\left.\frac{\partial^2 H^{\text{bulk}}}{\partial\boldsymbol{E}\partial\boldsymbol{\varepsilon}}\right|_{\mathrm{d}P_i=0}. \tag{61}$$

In this case the current phase field model reduces to the standard linear piezoelectric model with an extra term for the (constant) spontaneous polarization. In a Voigt notation (denoted by an underbar) with the index ordering $\{11,22,33,13,23,12\}$ one obtains

$$\underline{\mathbb{C}}^{E,P}=\begin{bmatrix} c_{11} & c_{12} & c_{13} & 0 & 0 & 0\\ c_{12} & c_{11} & c_{13} & 0 & 0 & 0\\ c_{13} & c_{13} & c_{33} & 0 & 0 & 0\\ 0 & 0 & 0 & c_{44} & 0 & 0\\ 0 & 0 & 0 & 0 & c_{44} & 0\\ 0 & 0 & 0 & 0 & 0 & c_{66}\end{bmatrix},\quad \underline{\boldsymbol{e}}^{P}=\begin{bmatrix} 0 & 0 & \bar{e}_{31}\\ 0 & 0 & \bar{e}_{31}\\ 0 & 0 & \bar{e}_{33}\\ 0 & \bar{e}_{15} & 0\\ \bar{e}_{15} & 0 & 0\\ 0 & 0 & 0\end{bmatrix}^{\mathrm{T}},\quad \underline{\boldsymbol{\epsilon}}^{\varepsilon,P}=\begin{bmatrix} \bar{\epsilon}_{11} & 0 & 0\\ 0 & \bar{\epsilon}_{11} & 0\\ 0 & 0 & \bar{\epsilon}_{33}\end{bmatrix} \tag{62}$$

with $c_{66}=\frac{1}{2}(c_{11}-c_{12})$. This means that the input values given in (51)–(54) are identical with the model response in the respective components of the material tensors (36), (37) in a Voigt notation, i.e. $\underline{\mathbb{C}}=\underline{\mathbb{C}}^{E,P}$, $\underline{\boldsymbol{e}}=\underline{\boldsymbol{e}}^{P}$, and $\underline{\boldsymbol{\epsilon}}=\underline{\boldsymbol{\epsilon}}^{\varepsilon,P}$. However, since the order parameter is allowed to change in phase field models, this option does not seem to be very sensible. Under the condition $\mathrm{d}\boldsymbol{\eta}=\boldsymbol{0}$ the moduli are defined by

$$\mathbb{C}^{E,\eta}=\left.\frac{\partial^2 H^{\text{bulk}}}{\partial\boldsymbol{\varepsilon}^2}\right|_{\mathrm{d}E_i=\mathrm{d}\eta_i=0},\quad \boldsymbol{\epsilon}^{\varepsilon,\eta}=-\left.\frac{\partial^2 H^{\text{bulk}}}{\partial\boldsymbol{E}^2}\right|_{\mathrm{d}\varepsilon_{ij}=\mathrm{d}\eta_i=0},\quad \boldsymbol{e}^{\eta}=-\left.\frac{\partial^2 H^{\text{bulk}}}{\partial\boldsymbol{E}\partial\boldsymbol{\varepsilon}}\right|_{\mathrm{d}\eta_i=0}. \tag{63}$$

As shown above, the internal micro-force $\boldsymbol{g}$ vanishes since we have a homogeneous problem. Then (14) implies

$$\boldsymbol{g}=-\beta\dot{\boldsymbol{P}}-\boldsymbol{\eta}=\boldsymbol{0}\quad\Rightarrow\quad\boldsymbol{\eta}=-\beta\dot{\boldsymbol{P}}=\frac{\partial H}{\partial\boldsymbol{P}}. \tag{64}$$

Since we postulate that $\mathrm{d}\boldsymbol{\eta}=\boldsymbol{0}$, we have to evaluate the moduli (63) at the point at which the system is equilibrated. The equilibrated state can be found iteratively by letting the system evolve due to the Ginzburg–Landau equation, which is given by $(64)_2$, until $\dot{\boldsymbol{P}}=\boldsymbol{0}$ is reached. Another possibility is to set $\beta=0$ so that the relaxed state is reached immediately (after one time step). Note however that with $\beta=0$ one loses the information about the time required for the system to evolve to the equilibrated state. Since this will be relevant just below, we take the first approach and solve the time-dependent problem.

Using just one finite element which is poled in the x_3-direction, i.e. $\boldsymbol{P}_0^*=[0,P_0]^{\mathrm{T}}$, we obtain the small-signal response by applying small electric fields and small strains in the sense of (63). That is to say, small increments in E_1,E_2, and $\varepsilon_{11},\varepsilon_{22}$ and ε_{12} with respect to the spontaneous strain $\boldsymbol{\varepsilon}^0=\boldsymbol{\varepsilon}^0|_{\boldsymbol{P}=\boldsymbol{P}_0^*}$ are applied one at a time in a successive manner. Here the model response is linear for electric fields below approximately 10^5 V/m and elastic strains no larger than about $10^{-3}\%$. The resulting dielectric, elastic, and piezoelectric moduli are shown in Fig. 2(a)–(c); each curve is normalized with respect to the respective input value for $BaTiO_3$ given in (51)–(54). The system becomes stationary after less than 20 ps, and the deviations of the effective material response from the input values are up to 300%. This is due to the fact that the primary and the secondary order parameter ($\boldsymbol{P}$ and $\boldsymbol{\varepsilon}^0$) change under the applied loading according to the evolution Eq. $(64)_2$. Note that the instantaneous response matches the input values as all graphs start at the point $(0,1)$. As we will see in Section 3.5, the time scale at which the material parameters evolve is much smaller than the time required for the evolution of a (rather elementary) microstructure. Therefore it seems reasonable to adjust the input

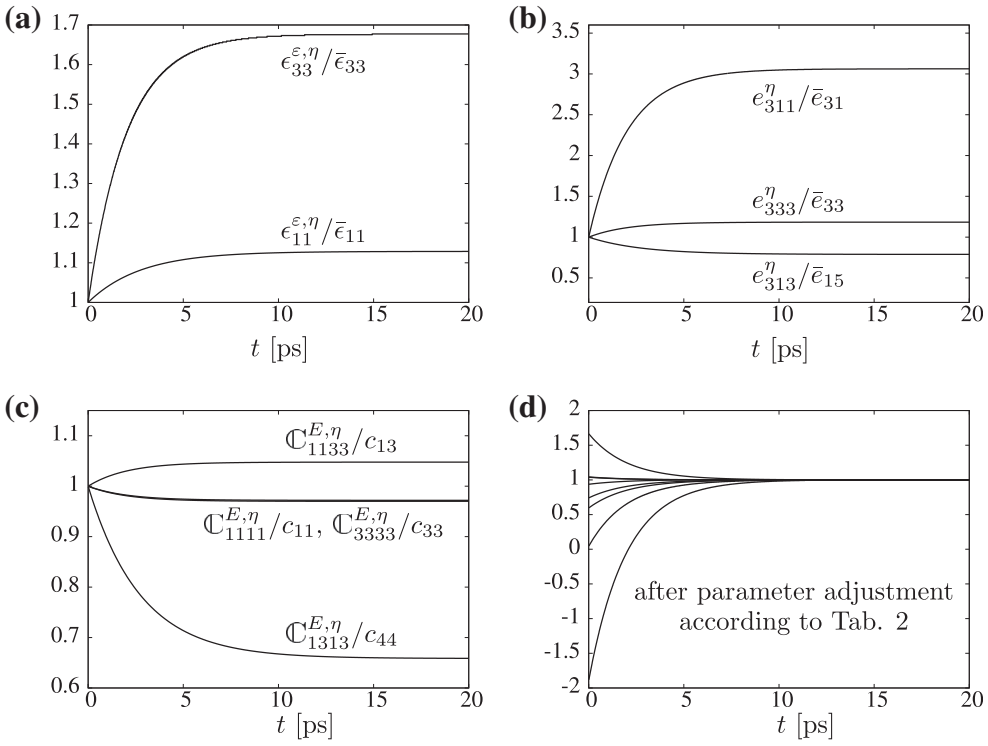

Fig. 2. (a)–(c) The numerically obtained tangent moduli approach stationary values as the order parameter evolves under small-signal loading. (d) After a correction of the input material parameters the linear model response reflects the actual material properties.

values for the condition of a vanishing micro-stress. The adjustment procedure can be undertaken manually within a couple of iteration steps. Initially the material parameters given in (51)–(54) are used as input values for the computation of the tangent moduli by means of Eq. (63). Then these input values are changed until the material response matches the initial input values. The result of this iteration procedure is shown in Table 2. As can be seen in the fourth column of the table, the material response matches the values given in the first column. Since we confine ourselves to 2d simulations, there is no response value for c_{12}. The values thus obtained shall be used for the remainder of the paper. Note that the adaption procedure is valid for arbitrary small-signal loading within the above-stated range as the model response is linear within the small-signal range.

3.3. Regularization of the stiffness and dielectric tensor

The material tensors $\mathbb{C}$ and $\boldsymbol{\epsilon}$ depend on the order parameter in a nonlinear way. As was pointed out in Völker et al. (2011, 2012), this can lead to a singular material tangent when main diagonal components of $\boldsymbol{\epsilon}$ or $\mathbb{C}$ vanish. This problem can occur in all phase field models and as soon as $\boldsymbol{\epsilon}$ and/or $\mathbb{C}$ depend on the order parameter; the same goes for phenomenological models in which the macroscopic polarization is treated as an internal variable which evolves over time, see e.g. Mehling et al. (2007) (where the issue of non-definiteness is however not explicitly addressed). It is then a matter of the specific formulation of the thermodynamic potential and the concrete values of the elastic and dielectric constants, whether or not one or several tensor components become zero and positive definiteness is lost. The present formulation allows for a regularization of $\boldsymbol{\epsilon}$ and $\mathbb{C}$ by adding the terms with $\gamma_3, \alpha_4, \alpha_5, \alpha_6$ in (29), all of which do not appear in Schröder and Gross (2004) or Keip et al. (2014). Which of these terms are needed is determined by the definitions in (33).

For $BaTiO_3$ we have $\bar{\epsilon}_{11} > \bar{\epsilon}_{33}$ so that with (38) and (33) we obtain

$$\boldsymbol{\epsilon} = \bar{\epsilon}_{33}\mathbf{1} - (\bar{\epsilon}_{11} - \bar{\epsilon}_{33})\left(\boldsymbol{p}\otimes\boldsymbol{p} - |\boldsymbol{p}|^2\mathbf{1}\right) \tag{65}$$

with the main diagonal components

$$\epsilon_{11} = \bar{\epsilon}_{33} + (\bar{\epsilon}_{11} - \bar{\epsilon}_{33})\frac{P_2^2 + P_3^2}{P_0^2}, \tag{66}$$

$$\epsilon_{22} = \bar{\epsilon}_{33} + (\bar{\epsilon}_{11} - \bar{\epsilon}_{33})\frac{P_1^2 + P_3^2}{P_0^2}, \tag{67}$$

$$\epsilon_{33} = \bar{\epsilon}_{33} + (\bar{\epsilon}_{11} - \bar{\epsilon}_{33})\frac{P_1^2 + P_2^2}{P_0^2}. \tag{68}$$

Since $\bar{\epsilon}_{11} > \bar{\epsilon}_{33}$, we have no vanishing permittivities on the main diagonal of $\boldsymbol{\epsilon}$; in fact, $\boldsymbol{\epsilon}$ stays positive definite for arbitrary values of $\boldsymbol{P}$. For materials other than $BaTiO_3$ it may be the case that $\bar{\epsilon}_{11} < \bar{\epsilon}_{33}$. Then the definition of $\boldsymbol{\epsilon}$ yields $\gamma_3 = 0$ and

$$\epsilon_{ii} = \bar{\epsilon}_{11} + (\bar{\epsilon}_{33} - \bar{\epsilon}_{11})\frac{P_i^2}{P_0^2} \quad \text{(no summation over } i\text{)} \tag{69}$$

which also guarantees that the permittivity is always positive. Had we used the form (69) with the values given in (54), we would have noticed that the ith main diagonal component ϵ_{ii} vanishes for $P_i \approx 1.01P_0$, i.e. very near the spontaneous phase.

Similarly one obtains for the mechanical stiffness with (43)

$$\mathbb{C}_{iiii} = \lambda + 2\mu + 2\frac{\alpha_1}{P_0^4}P_i^2|\boldsymbol{P}|^2 + 2\frac{\alpha_2}{P_0^4}P_i^4 + 2\frac{\alpha_3}{P_0^2}P_i^2 + 2\frac{\alpha_4}{P_0^6}P_i^4|\boldsymbol{P}|^2, \tag{70}$$

where there is no summation over i. If the α_4-term in (43) is omitted, the stiffness component $\mathbb{C}_{iiii}$ becomes zero near the spontaneous states. This is illustrated by the contour plot of $\mathbb{C}_{1111}$ in Fig. 3(a). At approximately $(0, 1.33P_0)$ the stiffness vanishes and becomes negative as the argument P_3 further increases. Moreover, the elasticity tensor loses its positive definiteness at the points for which $|\boldsymbol{P}|/P_0$ is approximately 1.23 or 1.28 (depending on whether the "input values" or the "adjusted values" in Table 2 are used). If the α_4-term is included, then $\mathbb{C}_{1111}$ stays positive for arbitrary polarization states, see the contour plot in Fig. 3(b).

3.4. Effect of the regularization on the material response

In the following we demonstrate that the phase field model produces pathological results if either $\alpha_4 = 0$ or $\gamma_3 = 0$ in (43) and (38), respectively. In order to elaborate the influence of these two terms, simulations are conducted first in the presence, then in absence of one of the two terms. In each case we use the "adjusted values" given in Table 2.

The first simulation concerns the α_4-term. The geometry and boundary conditions are sketched in Fig. 4(a). Since we are interested in homogeneous solutions only, we use just one finite element in the simulations. The electric potential is fixed so that there is no electric field within the element; the lateral boundaries are load free, i.e. $D_j n_j = 0, \sigma_{ij} n_j = 0$, and $\Sigma_{ij} n_j = 0$. Mechanically the system is loaded by a displacement u_0 resulting in an elastic strain of 1.25%; the bottom edge is kept at $u_3 = 0$. Rigid body movements are excluded by setting $u_1 = 0$ at the lower right node. The initial conditions are $\boldsymbol{P}_0^* = [0, 0, P_0]^{\mathrm{T}}, \boldsymbol{u}^* = \boldsymbol{0}$, and $\varphi^* = 0$. Once the simulation is started, the primary and secondary order parameter as well as $\mathbb{C}, \boldsymbol{e}$, and $\boldsymbol{\epsilon}$ evolve until thermodynamic equilibrium is reached. Fig. 4(b) shows the model response in terms of the evolution of P_3 and the elastic energy W^{ela} (which is normalized with respect to its initial value). Note that since the electric field vanishes, the bulk enthalpy H^{bulk} coincides with the elastic energy of the system. For $\alpha_4 = 0$ the elastic energy approaches zero and becomes negative if the strain is further increased (not depicted), which indicates a pathological model response as the elastic energy is by definition strictly non-negative. This pathology is regularized by including the α_4-term in the bulk enthalpy: the elastic energy now stays positive. The normalized order parameter component P_3/P_0 is plotted for the sake of comparison between the two model responses.

Using the problem setup sketched in Fig. 4(a) we rerun the previous simulations with and without the γ_3-term (while keeping the α_4-term in both cases). The prescribed displacement u_0 results in an elastic strain of 0.01%. The results in Fig. 5(a) and (b) show that the dielectric tensor loses its positive definiteness if $\gamma_3 = 0$. If on the contrary the γ_3-term is included, the values for ϵ_{11} and ϵ_{33} remain positive.

To further illustrate the possible pathologies that can occur if $\gamma_3 = 0$ we consider the setup sketched in Fig. 6(a). Again using just one finite element we apply three different electric fields E_3 at 0.5 MV/m, 1.0 MV/m, and 1.5 MV/m. The model responses in terms of the electric energy density $\Psi^{\mathrm{elec}} = \frac{1}{2}E_i\epsilon_{ij}E_j, \epsilon_{33}$, and ϵ_{11} are plotted in Fig. 6(b)–(d), respectively. If $\gamma_3 = 0$, the electric energy density becomes negative, and the dielectric tensor loses its positive definiteness; this is not the case in the presence of the regularizing γ_3-term.

3.5. Microstructure evolution

We close the article with some elementary microstructure simulations in order to demonstrate the capabilities of the presented model. The first simulation concerns an evolving polarization vortex in a $BaTiO_3$ nanodot. Ferroelectric nanodots are well studied in the context of phase field modeling, see e.g. Wang (2010), Wang and Su (2011), Wang et al. (2012), Kontsos and Landis (2012) and Song et al. (2013) for 2d and 3d simulations. In the present

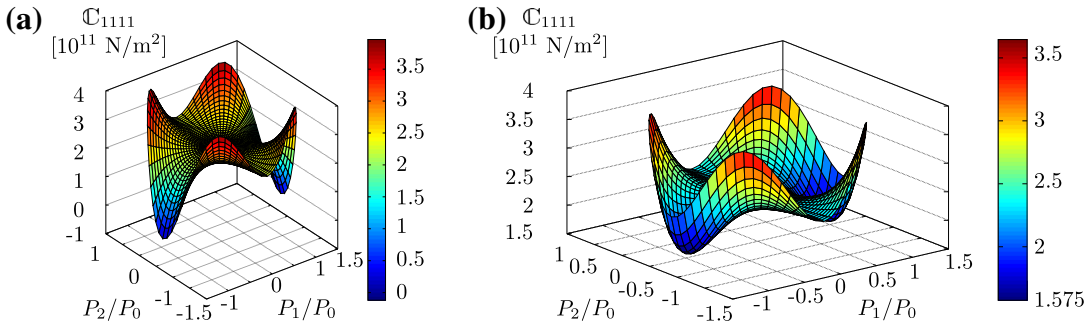

Fig. 3. (a) Contour plot of $\mathbb{C}_{1111}$ for the initial model formulation. The stiffness becomes negative in the vicinity of the spontaneous states $(0, \pm P_0)$. (b) This is corrected by regularizing the model so that $\mathbb{C}_{1111}$ is positive for all polarization states.

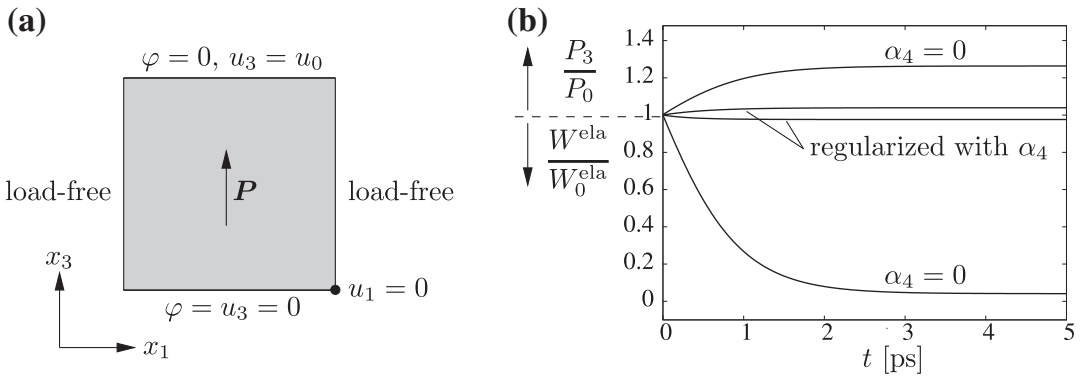

Fig. 4. (a) The poled phase is subjected to an elastic strain of 1.25%. (b) The elastic energy W^{ela} approaches zero in the absence of the α_4-term. The regularized model yields a positive definite elastic stiffness so that $W^{\mathrm{ela}} > 0$ if $\|\boldsymbol{\varepsilon} - \boldsymbol{\varepsilon}^0\| > 0$.

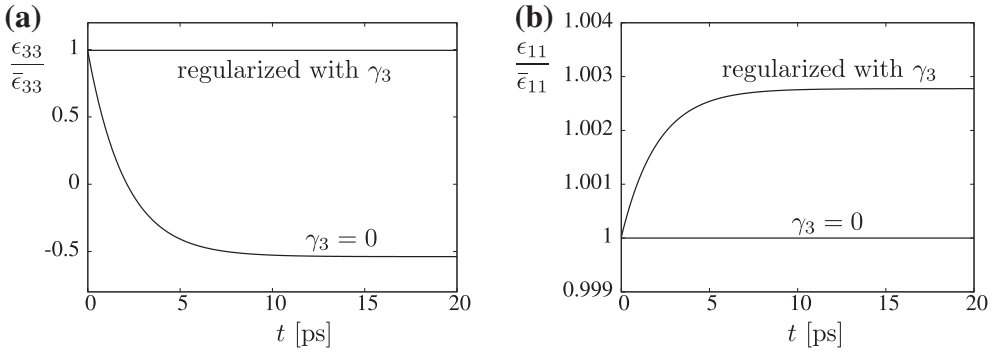

Fig. 5. For an elastic strain of 0.01% applied according to Fig. 4(a) the dielectric tensor becomes indefinite in the absence of the γ_3-term. The regularized model does not exhibit this pathological behavior.

simulation the dimensions of the nanodot are 15 nm × 10 nm with a mesh spacing of $\ell/3 = 0.5$ nm. The initial polarization is a random configuration which resembles a state just below the cubic-tetragonal phase transition, in short $|\boldsymbol{P}_0^*|/P_0 \ll 1$ with random orientations. The time step is kept constant at $\Delta t = 2$ ps throughout the simulation. At first the boundary conditions are load and charge free, i.e. $\sigma_{ij} n_j = 0$, $D_j n_j = 0$, and $\Sigma_{ij} n_j = 0$, the electric potential is fixed at just one node, and rigid body movements are excluded. The simulation is run until a stationary state is reached; then an electric field of 1 MV/m is applied in the vertical direction.

The microstructural evolution is visualized in the attached movie file `vortex.avi` in which four colors are used to indicate the direction of the order parameter. Additionally $\boldsymbol{P}(\boldsymbol{x}, t)$ is plotted as a vector field; the absolute values of the vectors are captured by the length and the gray-scale coloring of the arrows. For the discussion of the results we refer to the sequence of screenshots shown in Fig. 7(a)–(h). Once the simulation is started, the microstructure quickly forms a polarization vortex. Note, however, that the absolute value of the polarization is very small up to about $t = 100$ ps. Then, within the next 50 ps until $t = 150$ ps, the polarization rapidly increases and reaches the fully developed vortex at $t = 150$ ps. The system then requires a rather long period of time to reach the equilibrated state at $t = 0.5$ ns. At this point the electric field is activated, which causes the volume fractions of the vertically poled domains to increase at the expense of the laterally poled domains. Shortly after $t = 1$ ns there are only two domains left in the system, and the 180° domain wall is driven to the right boundary so that finally a monodomain state is reached (the video stops before this happens in order to be able to provide a high-quality movie with reasonable file size). The 180° domain wall

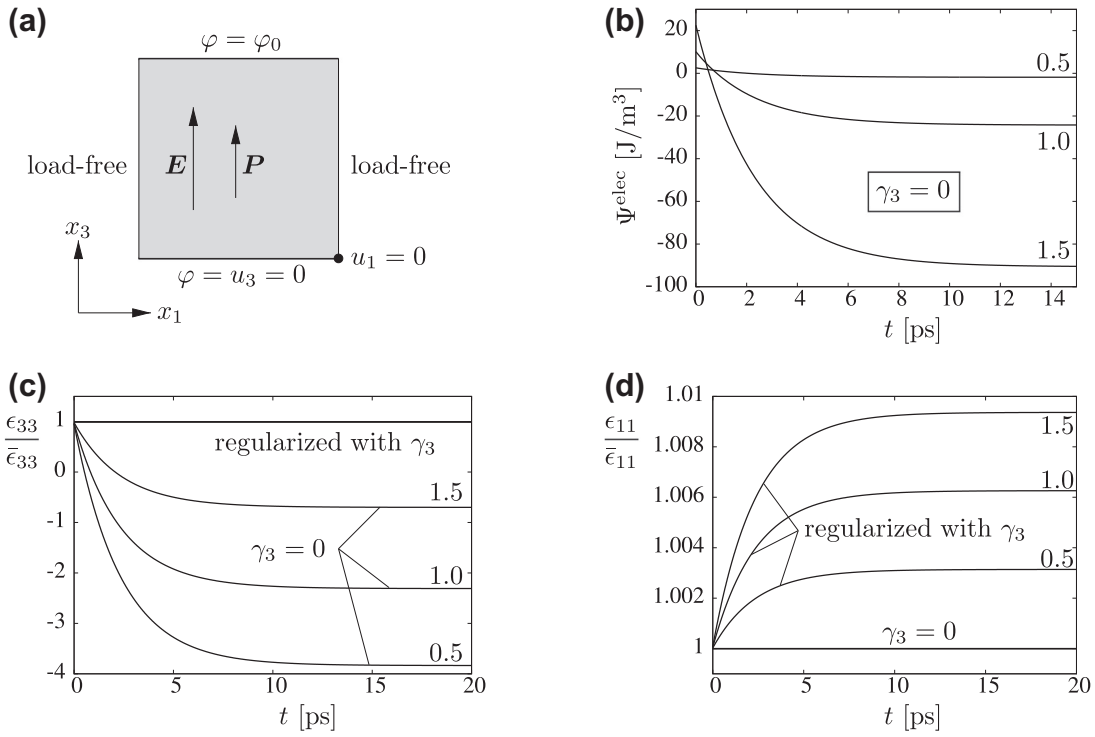

Fig. 6. (a) The poled crystal is subjected to different electric fields in the vertical direction. (b)–(d) The model responses for $E_3 = 0.5$ MV/m, 1.0 MV/m, and 1.5 MV/m illustrate the pathological character of the model if $\gamma_3 = 0$. The regularized model yields physically more acceptable results.

movement takes by far the longest time compared to the previous periods of the microstructure evolution. Note that the absolute times provided by the simulation scale directly with β^{-1}, the scalar inverse mobility constant in the Ginzburg–Landau equation. Having the function of an internal time scale, this parameter is only relevant if explicitly time-dependent external loading is applied, which we do not consider here. Finally it is noted that the use of the hypothetical lattice parameter a_{cub} at room temperature (cf. Section 3.1) results in stresses differing by roughly 10% while the evolution of the microstructures is qualitatively indistinguishable.

As another example we consider a $30\,\text{nm} \times 15\,\text{nm}$ free-standing nanodot with a horizontal crack. There are several ways to formulate the crack face conditions for piezoelectric materials: impermeable, permeable, semi-permeable, and energy consistent. For details the reader is referred to Landis (2004). Here we only consider the impermeable case which is defined by charge-free crack flanks. Starting with random initial conditions for $\boldsymbol{P}$ as in the previous simulation, we compare the microstructure evolution for (a) a charge-free boundary and (b) a setting where the top and bottom edges are kept at zero electric potential (the lateral sides and the crack faces are charge free in both cases). As in the previous simulation, a domain pattern emerges quickly while the final equilibrated state is reached only after a considerably longer time. The relaxed domain configurations for the two types of boundary conditions are shown in Fig. 8(a) and (b). The resulting microstructures are not symmetrical with respect to the crack plane since the random initial condition for $\boldsymbol{P}$ is non-symmetrical. Due to the charge-free crack face conditions the polarization aligns with the crack flanks. Note that the relaxed domain configurations depend on the applied boundary conditions. The polarization in Fig. 8(a) is aligned with the boundary due to $D_i n_i = 0$ on $\partial\mathcal{B}$ while this in not the case for $\varphi = 0$ at the top and bottom boundary in (b). These microstructures are consistent with phase field simulations given in Xu et al. (2010), although it must be noted that therein a different formulation of the phase field model as well as different material parameters were used. Simulations for a permeable crack can be found in Wang and Zhang (2007). The electric potential for the relaxed state is plotted in (c) and (d) for comparison.

The last simulation concerns a ferroelectric bi-crystal in which the crystal axes of one crystallite is rotated by 45° relative to the other, see the sketch in Fig. 9. Here x_1-x_3 is taken to be the global coordinate system. Note that the non-convex potential $\psi(\boldsymbol{P})$ in (44) assumes that the crystal axes coincide with the coordinate axes. Since this is not the case for the crystallite on the right hand side in Fig. 9, the primary variables $\boldsymbol{u}, \boldsymbol{P}$, and $\dot{\boldsymbol{P}}$ as well as the geometry data are transformed to the rotated local coordinate system x_1'–x_3' (the scalar field φ is invariant under this transformation). All derived quantities such as $\boldsymbol{\varepsilon}, \boldsymbol{\sigma}, \boldsymbol{E}, \boldsymbol{D}$ are then calculated with respect to the local coordinates. The resulting element residuals and element stiffness matrices are then back-transformed to the global coordinate system for subsequent assembly of the global system matrix and the global residual vector by the finite element program.

The grain boundary between the crystallites raises the question how the transition conditions should be formulated. While the displacement field and the electric potential may safely assumed to be continuous, it may be sensible to decouple the order parameter $\boldsymbol{P}$ at the grain boundary. Decoupling the order parameter means that $\boldsymbol{P}$ is allowed to be discontinuous across the grain boundary. Since the grain interface is assumed to be charge free, a jump in the component P_1 will have to be compensated by a depolarizing electric field; this is not necessary for jumps in the component P_2. Here we compare the two cases "coupled" and "decoupled" for a free-standing $24\,\text{nm} \times 18\,\text{nm}$ bi-crystal. The boundary conditions are charge free, and the initial conditions for $\boldsymbol{P}$ are as before small random perturbations around the cubic state. The resulting relaxed configurations is shown in Fig. 10(a) and (b). The two microstructures are qualitatively similar at the boundary due to the charge-free boundary condition; only the domain poled to the left at the

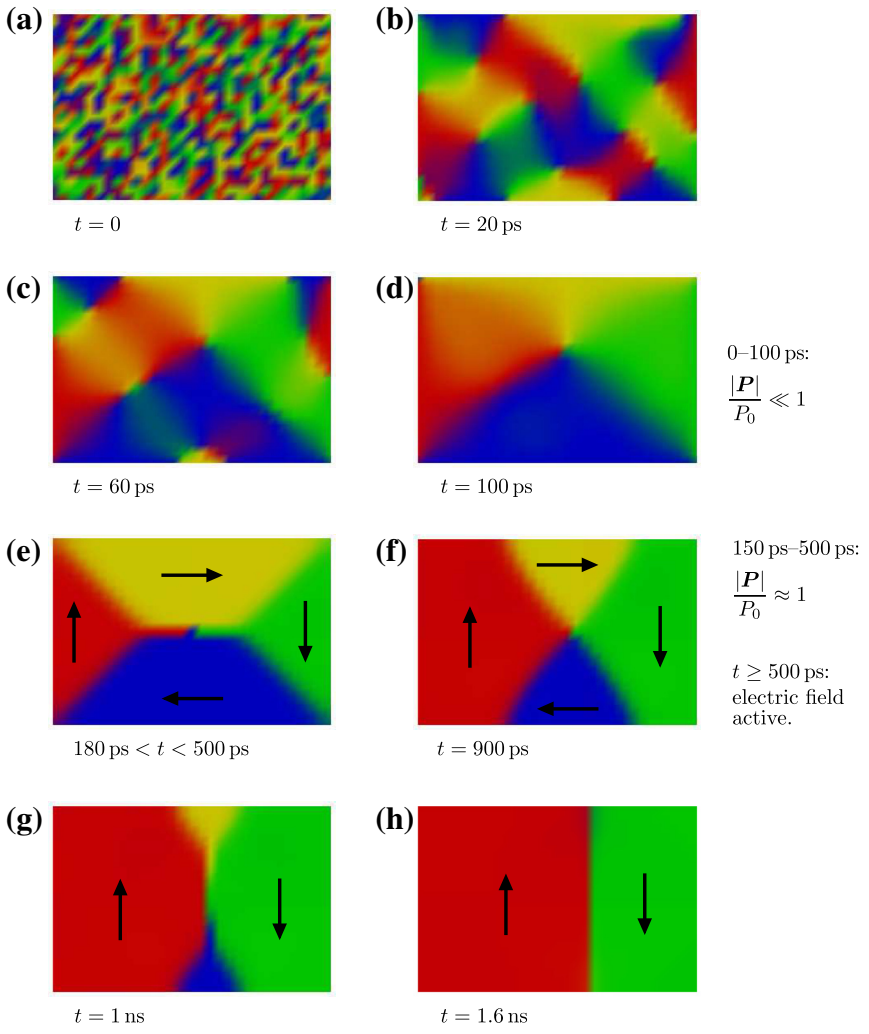

Fig. 7. Microstructure evolution starting from random initial polarization. A nanodot forms from $t = 0$ to $t = 180$ ps. Then an electric field of 1 MV/m is applied in the vertical direction, leading to the formation of a 180° domain wall which is eventually driven to the right border.

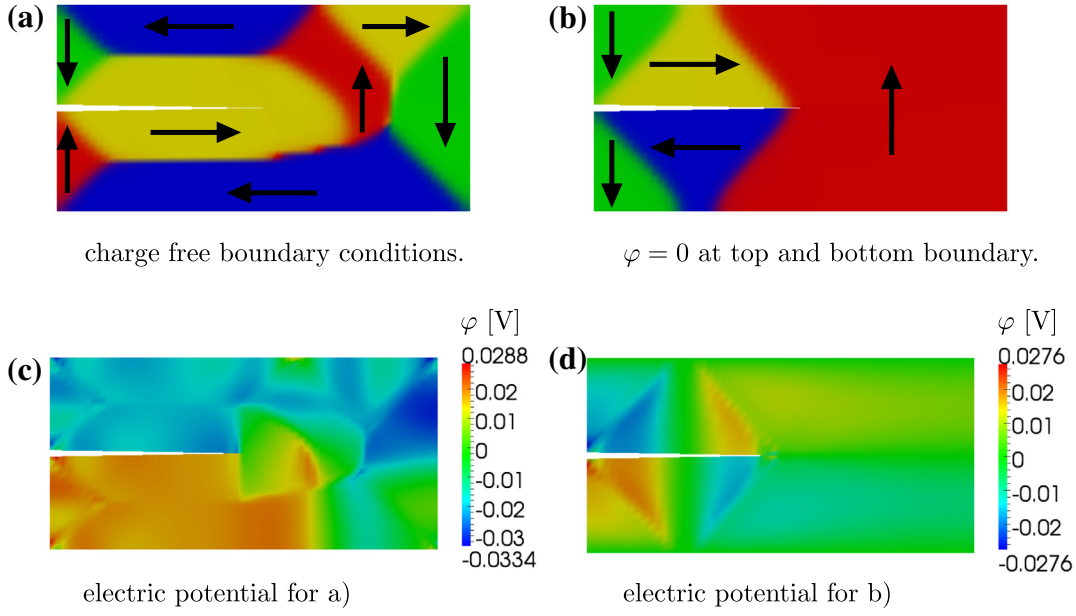

Fig. 8. (a), (b) Domain configurations for a cracked ferroelectric single crystal. (c), (d) electric potential for the two different applied boundary conditions.

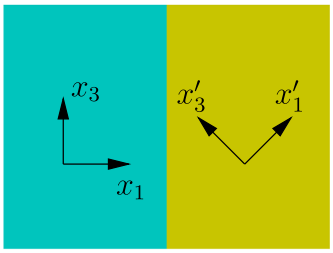

Fig. 9. Ferroelectric bi-crystal. The crystal axes x_1'–x_3' are rotated by 45° relative to crystal axes given by the x_1–x_3 coordinate system.

lower boundary in (a) is missing for the decoupled condition in (b). The decoupling of the order parameter leads to electric fields at the grain boundary which are not present if $\boldsymbol{P}$ is not decoupled, see Fig. 10(c) and (d) where the electric potential is plotted. While the electric displacement D_1 is continuous across the grain boundary (which was assumed to be charge free), the component D_2 exhibits a jump for the decoupled condition (e)–(h). In a future publication the authors intend to investigate the influence of the decoupled condition on the poling behavior of such a bi-crystal system and compare the results with the findings in Choudhury

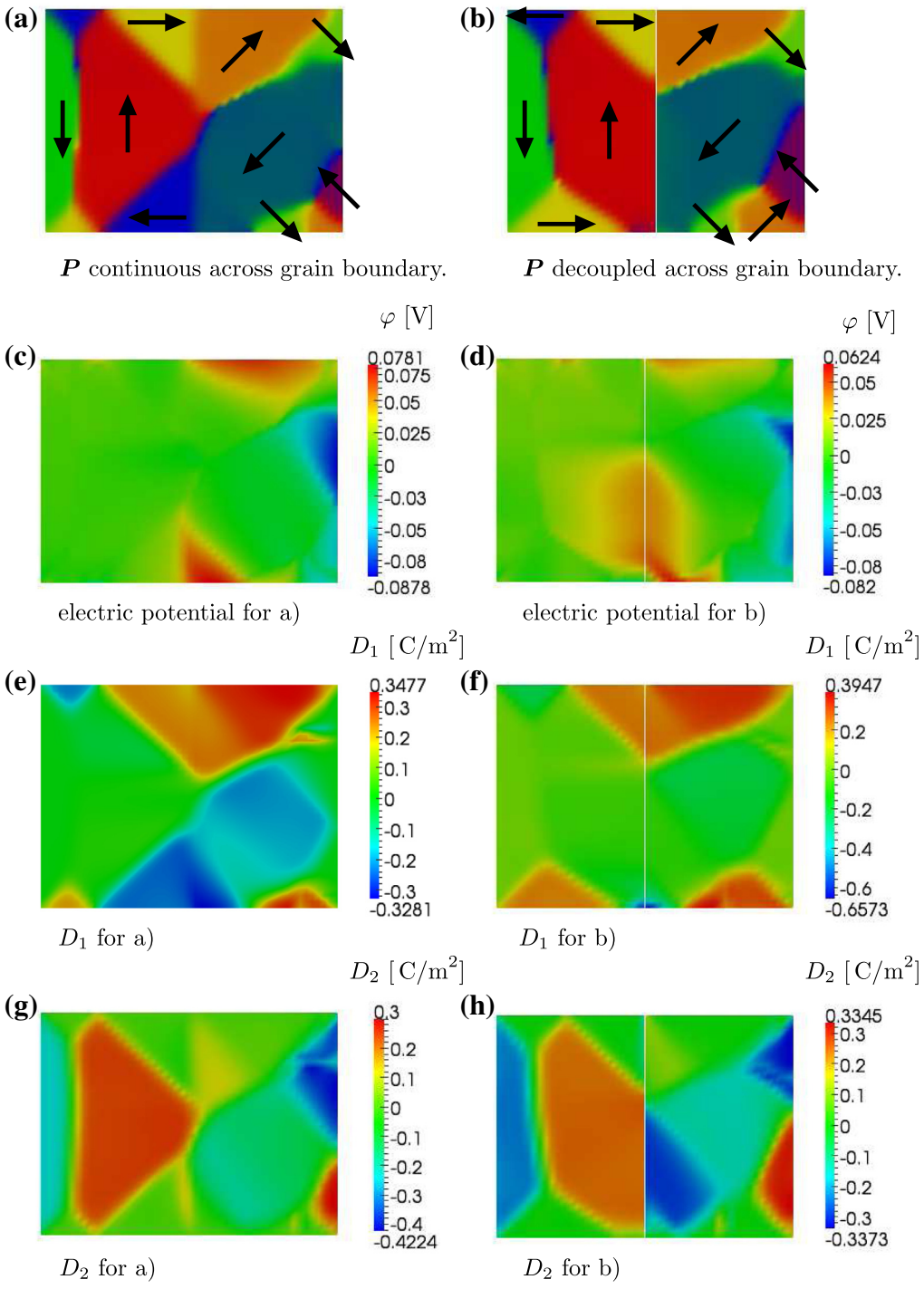

Fig. 10. Numerical results for the bi-crystal system. The plots on the left hand side were obtained for a continuous order parameter across the grain boundary; the results for a decoupled order parameter are shown on the right hand side for comparison.

et al. (2007); similar simulations can also be found in Zhang and Bhattacharya (2005b).

4. Conclusion

We presented a continuum phase field model for domain evolution in ferroelectric materials based on a micro-force thermodynamical framework from which a Ginzburg–Landau type evolution equation was derived. The electric enthalpy, which was used as the thermodynamic potential, was introduced in the form of classic linear piezoelectric theory on the one hand, and based on an invariant formulation for transverse isotropy on the other hand. Although both descriptions are equivalent, the invariant approach allowed for a consistent introduction of the order parameter-dependent material tensors. It was shown that the electric enthalpy used in Schröder and Gross (2004) had to be extended in order to prevent a loss of positive definiteness with regard to the mechanical stiffness and the dielectric tensor. After a reduction to 2d, the values of the material parameters were adapted under the condition of a vanishing micro-force (as opposed to a fixed primary order parameter).

The presented numerical simulations illustrate certain pathologies that arise if the electric enthalpy is not extended by additional regularizing terms. By considering both mechanical and electrical loading, it could be shown that the extended formulation does not exhibit the pathological behavior of the initial, unextended formulation. Finally a simulation of the formation of a polarization vortex in a $BaTiO_3$ nanodot was presented. The times required to evolve a vortex structure from a random initial state and subsequently to form a 180° domain wall in the presence of an electric field underlined the necessity to adjust the material parameters for the condition of a vanishing micro-force.

Appendix A. Supplementary data

Supplementary data associated with this article can be found, in the online version, at http://dx.doi.org/10.1016/j.ijsolstr. 2014.02.021.

References

Chen, L.-Q., 2008. Phase-field method of phase transformations/domain structures in ferroelectric thin films. J. Am. Ceram. Soc. 91 (6), 1835–1844.

Chen, L.Q., Shen, J., 1998. Applications of semi-implicit fourier-spectral method to phase field equations. Comput. Phys. Commun. 108, 147–158.

Choudhury, S., Li, Y.L., Krill III, C.E., Chen, L.-Q., 2007. Effect of grain orientation and grain size on ferroelectric domain switching and evolution: phase field simulations. Acta Mater. 55 (4), 1415–1426.

Schrade, D., Xu, B.X., Müller, R., Gross, D., 2008. On phase field modeling of ferroelectrics: parameter identification and verification. In: ASME Conf. Proc. (Smart Materials, Adaptive Structures and Intelligent Systems 2008), vol. 1. pp. 299–306.

Schrade, D., 2011. Microstructural modeling of ferroelectric material behavior (Ph.D. thesis). Technische Universität Kaiserslautern, Kaiserslautern.

Foeth, M., Sfera, A., Stadelmann, P., Buffat, P.-A., 1999. A comparison of HREM and weak beam transmission electron microscopy for the quantitative measurement of the thickness of ferroelectric domain walls. J. Electron Microsc. 48 (6), 717–723.

Fried, E., Gurtin, M.E., 1993. Continuum theory of thermally induced phase transitions based on an order parameter. Physica D 68 (3–4), 326–343.

Fried, E., Gurtin, M.E., 1994. Dynamic solid–solid transitions with phase characterized by an order parameter. Physica D 72 (4), 287–308.

Gurtin, M.E., 1996. Generalized Ginzburg–Landau and Cahn–Hilliard equations based on a microforce balance. Physica D 92 (3–4), 178–192.

Jona, F., Shirane, G., 1993. Ferroelectric Crystals. Dover Publications Inc, Mineola, New York.

Keip, M.-A., Thai, H., Schröder, J., Müller, R., Schrade, D., Gross, D., 2014. Phase-field simulation of transversely isotropic ferroelectrics during Piezoresponse Force Microscopy. Report 86, Institute of Mechanics, Department Civil Engineering, Faculty of Engineering, University of Duisburg-Essen.

Kontsos, A., Landis, C.M., 2012. Phase-field modeling of domain structure energetics and evolution in ferroelectric thin films. J. Appl. Mech. 77 (041014), 1–12.

Landis, C.M., 2004. Non-linear constitutive modeling of ferroelectrics. Curr. Opin. Solid State Mater. Sci. 8 (1), 59–69.

McMeeking, R.M., Landis, C.M., 2005. Electrostatic forces and stored energy for deformable dielectric materials. J. Appl. Mech. 72 (4), 581–590.

Mehling, V., Tsakmakis, C., Gross, D., 2007. Phenomenological model for the macroscopical material behavior of ferroelectric ceramics. J. Mech. Phys. Solids 55 (10), 2106–2141.

Merz, W.J., 1954. Domain formation and domain wall motions in ferroelectric BaTiO3 single crystals. Phys. Rev. 95 (3), 690–698.

Miehe, C., Zäh, D., Rosato, D., 2012. Variational-based modeling of micro-electro-elasticity with electric field-driven and stress-driven domain evolutions. Int. J. Numer. Methods Eng. 91 (2), 115–141.

Nowacki, W., 1979. Foundations of linear piezoelectricity. In: Parkus, H. (Ed.), Electromagnetic interactions in elastic solids. Springer, pp. 105–157.

Padilla, J., Zhong, W., Vanderbilt, D., 1996. First-principles investigation of 180° domain walls in BaTiO3. Phys. Rev. B 53 (10), R5969–R5973.

Schrade, D., Mueller, R., Xu, B.X., Gross, D., 2007. Domain evolution in ferroelectric materials: a continuum phase field model and finite element implementation. Comput. Methods Appl. Mech. Eng. 196 (41–44), 4365–4374.

Schrade, D., Müller, R., Gross, D., 2013. On the physical interpretation of material parameters in phase field models for ferroelectrics. Arch. Appl. Mech. 83, 1393–1413.

Schröder, J., Gross, D., 2004. Invariant formulation of the electromechanical enthalpy function of transversely isotropic piezoelectric materials. Arch. Appl. Mech. 73, 533–552.

Scott, J.F., 2007. Applications of modern ferroelectrics. Science 315 (5814), 954–959.

Song, Y.C., Ni, Y., Zhang, J.Q., 2013. Phase field model of polarization evolution in a finite ferroelectric body with free surfaces. Acta Mech. 224 (6), 1309–1313.

Stemmer, S., Streiffer, S.K., Ernst, F., Rühle, M., 1995. Atomistic structure of 90° domain walls in ferroelectric PbTiO3 thin films. Philos. Mag. A 71 (3), 713–724.

Su, Y., Landis, C.M., 2007. Continuum thermodynamics of ferroelectric domain evolution: theory, finite element implementation, and application to domain wall pinning. J. Mech. Phys. Solids 55 (2), 280–305.

Su, Y., Chen, H., Li, J.J., Soh, A.K., Weng, G., 2011. Effects of surface tension on the size-dependent ferroelectric characteristics of free-standing BaTiO3 nano-thin films. J. Appl. Phys. 110 (084108), 1–6.

Taylor, R.L., 2013. FEAP – A Finite Element Analysis Program, <http://www.ce.berkeley.edu/projects/feap/>.

Völker, B., Kamlah, M., 2012. Large-signal analysis of typical ferroelectric domain structures using phase-field modeling. Smart Mater. Struct. 21 (055013), 1–10.

Völker, B., Marton, P., Elsässer, C., Kamlah, M., 2011. Multiscale modeling for ferroelectric materials: a transition from the atomic level to phase-field modeling. Continuum Mech. Thermodyn. 23, 435–451.

Völker, B., Landis, C.M., Kamlah, M., 2012. Multiscale modeling for ferroelectric materials: identification of the phase-field model's free energy for PZT from atomistic simulations. Smart Mater. Struct. 21 (035025), 1–10.

Wang, J., 2010. Switching mechanism of polarization vortex in single-crystal ferroelectric nanodots. Appl. Phys. Lett. 97 (192901), 1–3.

Wang, J., Su, Y., 2011. Stability of polarization vortices within two interacting ferroelectric nanoparticles. Phys. Lett. A 375, 1019–1022.

Wang, J., Wang, T.Y., 2012. Phase field study of polarization vortex in ferroelectric nanostructures. J. Adv. Dielectr. 2 (2), 1241002–1–13.

Wang, J., Zhang, T.-Y., 2007. Phase field simulations of polarization switching-induced thoughening in ferroelectric ceramics. Acta Mater. 55, 2465–2477.

Xu, Y., 1991. Ferroelectric Materials and Their Applications. Elsevier Science Publishers B.V, Amsterdam.

Xu, B.X., Schrade, D., Gross, D., Müller, R., 2010. Phase field simulation of domain structures in cracked ferroelectrics. Int. J. Fract. 165, 163–173.

Xu, F., Wang, J.J., Sheng, G., Huang, E., Cao, Y., Huang, H.H., Munroe, P., Mahjoub, R., Li, Y.L., Nagarajan, V., Chen, L.Q., 2013. Phase field simulations of ferroelectrics domain structures in PbZrxTi1-xO3 bilayers. Acta Mater. 61, 2909–2918.

Zgonik, M., Bernasconi, P., Duelli, M., Schlesser, R., Günter, P., Garrett, M.H., Rytz, D., Zhu, Y., Wu, X., 1994. Dielectric, elastic, piezoelectric, electro-optic, and elasto-optic tensors of BaTiO3 crystals. Phys. Rev. B 50 (9), 5941–5950.

Zhang, W., Bhattacharya, K., 2005a. A computational model of ferroelectric domains. Part I: model formulation and domain switching. Acta Mater. 53 (1), 185–198.

Zhang, W., Bhattacharya, K., 2005b. A computational model of ferroelectric domains. Part II: grain boundaries and defect pinning. Acta Mater. 53, 199–209.